

# Nonlinear Network Reconstruction by Pairwise Time-delayed Transfer Entropy

Kai Chen<sup>1,2,3,4†</sup>, Zhong-qi K. Tian<sup>1,2,3,4†</sup>, Yifei Chen<sup>1,2,3,4</sup>, Songting Li<sup>1,2,3,4\*</sup>,  
Douglas Zhou<sup>1,2,3,4\*</sup>

<sup>1</sup>School of Mathematical Sciences, Shanghai Jiao Tong University, Shanghai, 200240, China.

<sup>2</sup>Institute of Natural Sciences, Shanghai Jiao Tong University, Shanghai, 200240, China.

<sup>3</sup>Ministry of Education Key Laboratory of Scientific and Engineering Computing, Shanghai Jiao Tong University, Shanghai, 200240, China.

<sup>4</sup>Shanghai Frontier Science Center of Modern Analysis, Shanghai Jiao Tong University, Shanghai, 200240, China.

\*Corresponding author(s). E-mail(s): [songting@sjtu.edu.cn](mailto:songting@sjtu.edu.cn); [zdz@sjtu.edu.cn](mailto:zdz@sjtu.edu.cn);

Contributing authors: ;

†These authors contributed equally to this work.

## Abstract

Analyzing network structural connectivity is crucial for understanding dynamics and functions of complex networks across disciplines. In many networks, structural connectivity is not observable, which requires to be inferred via causal inference methods. Among them, transfer entropy (TE) is one of the most broadly applied causality measure due to its model-free property. However, TE often faces the curse of dimensionality in high-dimensional probability estimation, and the relation between the inferred causal connectivity and the underlying structural connectivity remains poorly understood. Here we address these issues by proposing a pairwise time-delayed transfer entropy (PTD-TE) method. We theoretically establish a quadratic relationship between PTD-TE values and node coupling strengths, and demonstrate its immunity to dimensionality issues and broad applicability. Tests on biological neuronal networks, nonlinear physical systems, and electrophysiological data show PTD-TE achieves consistent, high-performance reconstructions. Compared to a bunch of existing approaches for network connectivity reconstruction, PTD-TE outperforms these methods across various network systems in accuracy and robustness against noise. Our framework provides a scalable, model-agnostic tool for structural connectivity inference in nonlinear real-world networks.

**Keywords:** causal inference, transfer entropy, network reconstruction, curse of dimensionality

## Introduction

The structure of complex networks is crucial for understanding of network dynamics in many scientific fields such as neuroscience [1] and climatology [2]. However, technological limitations often constrain the size and scale of direct network structure measurements, necessitating the use of reconstruction methods based on node activity time series. When limited knowledge of the underlying dynamics is given, it's almost impossible to reconstruct the network's structural connectivity directly from the time series data of individual nodes' activity using model-based methods such as dynamic causal modeling [3] and Granger causality (GC) analysis

[4–6]. Alternatively, one may resort to statistical approaches attempting to obtain the causal connectivity from model-free perspectives [7–11]. An appealing causal inference method that attracts great interest is transfer entropy (TE) [12–17]. For the causal interaction given by  $X \rightarrow Y$ , the uncertainty about  $Y$ ’s future can be reduced by taking  $X$ ’s history into account. This reduction of uncertainty is quantified by the TE value as an information-theoretic measure. Because of its conceptional simplicity and model-free property, TE has been used for detecting causal connectivity in many fields, *e.g.*, finance, neuroscience, and social science [13, 14, 18, 19].

However, the *effective connectivity* estimated by TE-inferred information-transfer depends on nodes’ activity [20], and it remains ambiguous on its quantitative relation with the *structural connectivity* of a system [1, 21]. Previously, works have established a direct link between the GC-inferred effective connectivity and the underlying structural connectivity for linear systems [22] with extensions to nonlinear systems [23, 24]. Although TE is equivalent to GC for Gaussian random variables [25], the theoretical framework for quantitatively linking the TE-inferred effective connectivity to structural connectivity remains largely unexplored.

Additionally, TE suffers from the curse of dimensionality computationally. Considering a two-node system  $X \rightarrow Y$ , the core step of TE computation requires estimating the joint probability distribution of nodes’ history. According to the Markovian property, nodes with longer memory dependencies necessitate considering a longer history [12, 26], leading to a rapid increase in the dimensionality of the joint probability distribution. This results in an exponential growth in the data volume required for estimation, causing the curse of dimensionality. To address this issue, previous works have pursued two strategies: reducing the number of states by replacing raw data with its ordinal symbolization in the delayed embedding [27–29], and improving high-dimensional distribution estimation using methods such as  $k$ -nearest neighbors estimators [14, 30–32] and kernel density estimators [30, 33, 34]. However, these strategies cannot fully overcome the high-dimensional nature of the joint probability distribution caused by the long temporal dependencies in the data.

Moreover, in networks with multiple interacting nodes, conditional TE (CTE) or partial TE [35–37] is introduced to isolate direct interactions from interference caused by indirect causal effects. However, CTE estimation requires computing the joint probability distribution of historical data of all nodes, further exacerbating the curse of dimensionality. Previous works have attempted to reduce the extra dimensionality introduced by CTE using graphical models based on prior knowledge of the system. First, leveraging network sparsity reduces the number of intermediate nodes considered in CTE [38, 39]. Second, under the assumption of first-order Markov chains, direct interactions can be approximated using an iterative algorithm for pairwise TE with a first-order time delay [40]. However, these additional assumptions limit the method’s applicability to general nonlinear systems, and the choice of hyperparameters remains underexplored. As a result, the computational challenge of the curse of dimensionality remains unresolved, as reviewed in [17].

In this work, we resolve the aforementioned challenges for TE-based network reconstruction by proposing a novel pairwise time-delayed transfer entropy (PTD-TE) and establishing the theoretical foundation for its success. Using the classical Hodgkin-Huxley (HH) neuronal network [41–43] as a primary example, we demonstrate that PTD-TE, estimated from binarized neuronal voltage time series (neuronal spike trains), accurately matches the network’s structural connectivity, enabling precise reconstruction. We prove a quadratic relationship between PTD-TE values and inter-neuronal coupling strength and explain how PTD-TE overcomes the curse of dimensionality by leveraging the auto-correlation structure of binary time series, pairwise inference, and an additional time delay parameter. The framework’s success extends to other nonlinear networks, such as the Lorenz system [44, 45] and discrete logistic map [46, 47]. Compared to other existing methods, PTD-TE outperforms across multiple benchmark systems. Finally, we apply PTD-TE to real spike trains using multiple public datasets from Allen Institute [48–50]. Consistent reconstructions across different brain state conditions validate PTD-TE’s effectiveness on experimental data. Our work provides an operable and efficient model-free framework for inferring network structural connectivity from recorded node activity time series, and offers insights into the relationship between structural connectivity, information flow, and functional properties in general nonlinear networks.

## Results

### Pairwise time-delayed transfer entropy

To better introduce PTD-TE, we first revisit the definition of CTE. Taking a nonlinear network of  $s + 2$  nodes as an example, node  $X$  and  $Y$  are two different nodes in the network, and  $Z_i$ , ( $i = 1, 2, \dots, s$ ) is one of the resting nodes.  $\{x_n\}$ ,  $\{y_n\}$ , and  $\{z_{i,n}\}$  are the time series of nodes' activity of  $X$ ,  $Y$ , and  $Z_i$ , respectively. The CTE from  $X$  to  $Y$  is defined as follows:

$$T_{X \rightarrow Y}^{\text{cond}} = \sum_{y_{n+1}, y_n^{(k)}, x_n^{(l)}, z_{1,n}^{(k_1)}, \dots, z_{s,n}^{(k_s)}} p\left(y_{n+1}, y_n^{(k)}, x_n^{(l)}, z_{1,n}^{(k_1)}, \dots, z_{s,n}^{(k_s)}\right) \log \frac{p(y_{n+1} | y_n^{(k)}, x_n^{(l)}, z_{1,n}^{(k_1)}, \dots, z_{s,n}^{(k_s)})}{p(y_{n+1} | y_n^{(k)}, z_{1,n}^{(k_1)}, \dots, z_{s,n}^{(k_s)})}, \quad (1)$$

where  $y_{n+1}$  is the current state of  $Y$ , and  $y_n^{(k)} := [y_n, y_{n-1}, \dots, y_{n-k+1}]$ ,  $x_n^{(l)} := [x_n, x_{n-1}, \dots, x_{n-l+1}]$ , and  $z_{i,n}^{(k_i)} := [z_{i,n}, z_{i,n-1}, \dots, z_{i,n-k_i+1}]$  represents the historical activity of  $Y$ ,  $X$ , and  $Z_i$ , respectively.  $k$  and  $l$  are the order parameter of  $X_n$  and  $Y_n$ , respectively, representing the number of discrete history time point, while  $k_i$  is the order parameter for  $Z_{i,n}$ .

In contrast to CTE, the PTD-TE from  $X$  to  $Y$  is defined as follows:

$$T_{X \rightarrow Y}^{\text{PTD}}(k, l, \tau) = \sum_{y_{n+1}, y_n^{(k)}, x_n^{(l)}} p\left(y_{n+1}, y_n^{(k)}, x_{n-\tau}^{(l)}\right) \log \frac{p\left(y_{n+1} | y_n^{(k)}, x_{n-\tau}^{(l)}\right)}{p\left(y_{n+1} | y_n^{(k)}\right)}, \quad (2)$$

where  $\tau$  is parameter of time delay, and  $y_{n+1}$  is the current state of  $Y$ , and  $y_n^{(k)}$  and  $x_{n-\tau}^{(l)}$  are defined similarly as those in CTE.  $k$  and  $l$  are the order parameters for  $Y$  and  $X$ , respectively.

Here, we highlight three key differences between PTD-TE and CTE that overcome the curse of dimensionality. First, instead of applying to continuous-valued time series, PTD-TE is specifically designed for binary times series, such as spike-train data widely analyzed in the neuroscience field. This allows for a smaller  $k$  order, significantly reducing the number of states in the joint probability state space (the reason is discussed in detail later). Second, PTD-TE emphasizes pairwise analysis, ensuring broader applicability for large networks with multi-nodes. In real experiments, sparse recordings often provide access only to subnetworks. PTD-TE's independence from third-node activity enables reconstruction of subnetworks even when  $\{z_{i,n}\}$  ( $i = 1, \dots, s$ ) are not fully available, bypassing issues caused by the hidden nodes and substantially reducing the dimensionality of the joint probability space. Finally, inspired by information-transfer delays [29], we introduce an extra delay parameter  $\tau$  to further reduce the order parameter  $l$  in practical applications. Note that only for a two-node network with  $\tau = 0$ , PTD-TE reduces to classical TE, applied to binary time series.

### Network reconstruction pipeline using PTD-TE

We develop a framework to reconstruct the structural connectivity (*i.e.*, the network's adjacency matrix) using PTD-TE-estimated effective connectivity. This involves a binary classification problem to distinguish directly connected node pairs. First, we compute PTD-TE values for all possible node pairs in a network. For a given ordered pair, say  $X \rightarrow Y$ , we determine PTD-TE parameters  $k$ ,  $l$  and  $\tau$  through the following pipeline, as shown in Fig. 1: (i) convert continuous-valued time series  $\{x_n\}$  and  $\{y_n\}$  to spike trains by thresholding, and then binarize it using discrete time step  $\Delta t$ , (ii) compute the autocorrelation function (ACF) of the binarized  $\{y_n\}$  to select  $k = \hat{k}$ , (iii) estimate the optimal delay  $\tau = \hat{\tau}$  using  $\hat{\tau} = \arg \max_{\tau} T_{X \rightarrow Y}^{\text{PTD}}(\hat{k}, l = 1, \tau)$ , and (iv) choose  $l$  based on interaction dynamics (*e.g.*,  $l = 1$  for most cases; higher for weak and persistent interactions) (see *Methods*).

Next, we fit a Gaussian mixture model (GMM) (double-mixture) to the distribution of PTD-TE value across all pairs. The binary classification threshold, derived from this model, identifies directly connected pairs as with PTD-TE values above the threshold.

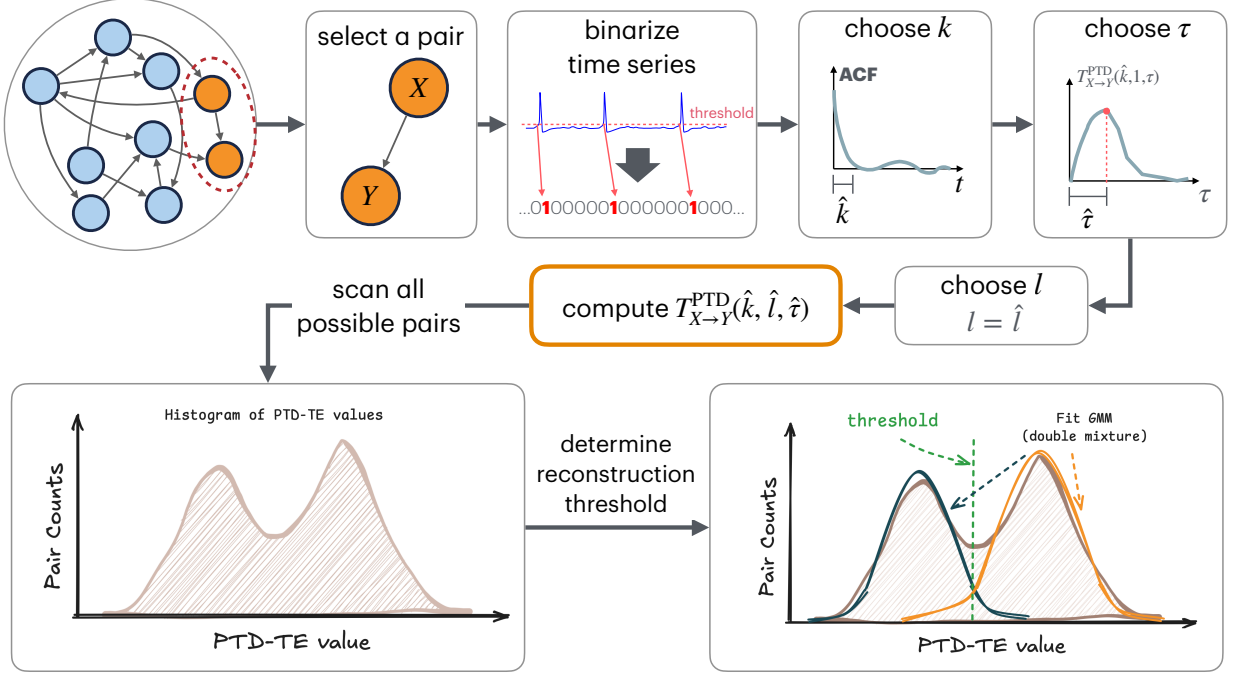


**Fig. 1** Schematics of PTD-TE reconstruction pipeline.

## Reconstructing Hodgkin-Huxley neuronal networks

We test the effectiveness of PTD-TE-based network reconstruction using the classical Hodgkin-Huxley (HH) neuronal network model [41], investigating the relationship between PTD-TE-inferred effective connectivity and structural connectivity. The HH model, one of the most widely used biophysical neuronal models, quantitatively describes the ionic mechanisms of membrane potential dynamics and action potential generations. By analyzing HH neuronal networks, we can validate PTD-TE’s potential applicability to real neural recordings.

We first build a three-neuron HH network connected with the chain motif, as shown in Fig. 2a-b, simulating it using a fourth-order Runge-Kutta scheme. The spike times of neurons,  $\{T_{ik}\}$  ( $i = 1, 2, 3$ ), are recorded (see HH model details in *Methods*). With a proper time step  $\Delta t = 0.5$  ms, we convert the spike trains into binary time series  $S_i(t)$ , where  $S_i(t) = 1$  indicates that  $i$ -th neuron fires a spike within  $[t + \Delta t]$ , and  $S_i(t) = 0$  otherwise. We address that the spiking nature of neurons and synaptic interactions enables this continuous-to-binary conversion of neurons’ voltages, which inspired the binarization step in the PTD-TE-reconstruction pipeline originally. We later demonstrate its extension to non-neuronal network systems.

Following the PTD-TE reconstruction pipeline (Fig. 1), the estimated PTD-TE values align closely with the structural connectivity pattern, *i.e.*, the adjacency matrix (Fig. 2c). Notably, PTD-TE values for connected neuron pairs ( $X \rightarrow Y$  or  $Y \rightarrow Z$ ) are significantly larger - often by orders of magnitude - than those for unconnected pairs ( $X \rightarrow Z$ ). To access robustness, we simulate multiple realizations of the three-neuron system by varying Poisson input parameters (input strength  $f$  and input frequency  $\nu$ ), which primarily control the system’s dynamical regime. We then evaluate the ratios  $T_{X \rightarrow Y}^{\text{PTD}}/T_{X \rightarrow Z}^{\text{PTD}}$ . As shown in Fig. 2d, this ratio consistently exceeds 100 across diverse dynamical regimes, *i.e.*,  $T_{X \rightarrow Y}^{\text{PTD}}$  for the connected pair is at least 2 orders of magnitude larger than  $T_{X \rightarrow Z}^{\text{PTD}}$  for the unconnected pair. This robust performance of PTD-TE effectively distinguish connected pairs from those indirectly interacting ones, ensuring reliable network reconstruction. We further evaluate PTD-TE on a three-neuron HH network with a confounder motif (Fig. 2e-f), where one neuron influences two others without direct interaction between them. Consistent with previous results, PTD-TE effectively distinguishes direct connections from indirect ones, as demonstrated in Fig. 2g-h.

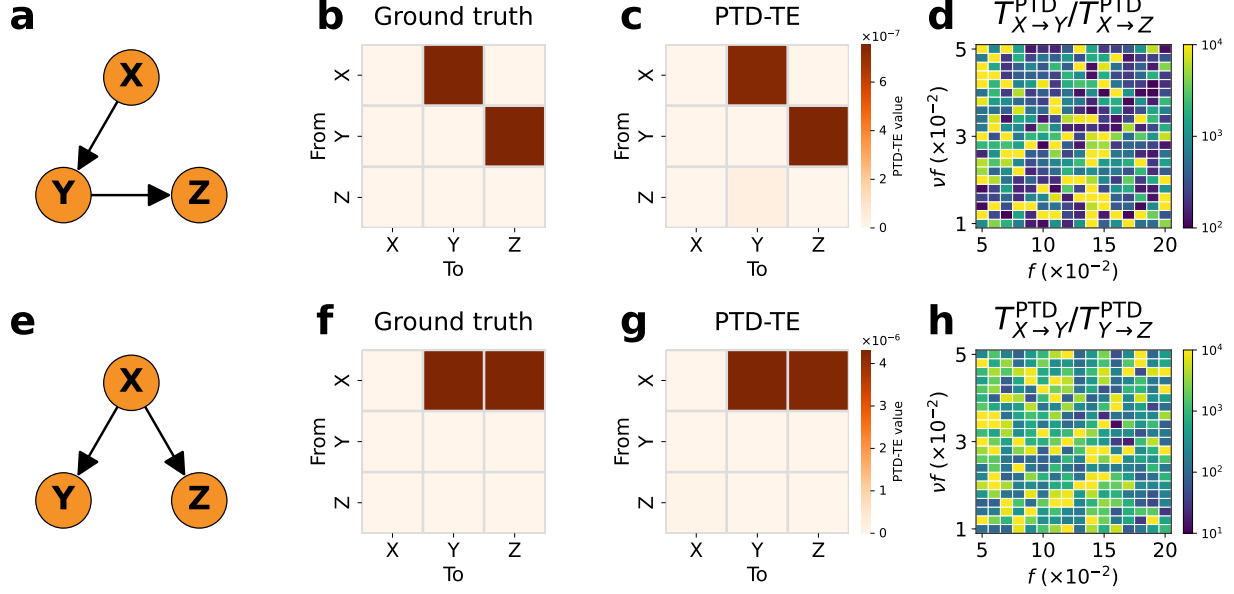


**Fig. 2** Two typical motifs of 3-HH neuron networks and the corresponding reconstruction performance by PTD-TE. **a.** The graph of a 3-neuron network with chain motif. **b.** The adjacency matrix for the network in **a.** **c.** The matrix of inferred PTD-TE values for the network in **a.** **d.** The ratio of PTD-TE values between connected and unconnected pairs. The minimum ratio in **d** is greater than 100, across a broad dynamical regime with firing rates from 2 to 50 Hz. **e-h.** Similar results for a 3-neuron network with confounder motif. The minimum ratio in **h** is greater than 10. In these cases, 2.7 hours neuronal recordings are used for PTD-TE estimation. PTD-TE parameters are chosen as  $k = 1$ ,  $l = 1$ , and  $\tau = 3$  ms, following the pipeline in Fig. 1.

## Mechanisms underlying PTD-TE reconstruction

The remarkable effectiveness of PTD-TE reconstruction motivates us to explore its underlying mechanism. First, the consistent alignment between PTD-TE values and structural connectivity suggests a quantitative relationship between them, which we explore further. Second, unlike conventional TE and CTE, PTD-TE avoids the curse of dimensionality, which typically arises when applying conventional TE to continuous-valued time series.

### PTD-TE correlates with network coupling strength

We next derive the relationship between PTD-TE and network coupling strength by considering a two-neuron network with a unidirectional connection ( $X \rightarrow Y$ ). To simplify the notation, we first map each binary number sequence of  $y_n^{(k)}$  and  $x_{n-\tau}^{(l)}$  in Eq. (2) to a decimal number (*e.g.*, the state  $[1,0,0]$  is mapped to 4 as decimal number representation). And for simplicity, we denote

$$p_{a,b} = p(y_{n+1} = 1 | y_n^{(k)} = a, x_{n-\tau}^{(l)} = b) \quad \text{and} \quad \Delta p_{a,b} = p_{a,b} - p_{a,0},$$

where  $a$  and  $b$  are decimal numbers representing the state of  $y_n^{(k)}$  and  $x_{n-\tau}^{(l)}$ , respectively. Note that  $\Delta p_{a,b}$  reflects the activity induced change of state probability of  $y_{n+1} = 1$  given the non-quiescent  $x_{n-\tau}^{(l)}$  state, which depends on coupling strength  $S$ . Subsequently, we can rewrite PTD-TE expression (Eq. (2)) in terms of  $p_{a,b}$  and  $\Delta p_{a,b}$  with a Taylor expansion form:

$$T_{X \rightarrow Y}^{\text{PTD}} = \frac{1}{2} \sum_a \frac{1}{p_{a,0} - p_{a,0}^2} \left\{ \sum_b p(a,b) \Delta p_{a,b}^2 - \frac{[\sum_b p(a,b) \Delta p_{a,b}]^2}{p(a)} \right\} + o(\Delta p_{a,b}^2), \quad (3)$$

where  $p(a, b) = p(y_n^{(k)} = a, x_{n-\tau}^{(l)} = b)$  and  $p(a) = p(y_n^{(k)} = a)$  (see *Methods* for derivation details). From Eq. (3), we reveal that PTD-TE value is quadratically related to  $\Delta p_{a,b}$ . We then show  $\Delta p_{a,b}$  can be Taylor expanded with respect to coupling strength  $S$  (see *Methods*), with a non-vanishing first-order leading term, *i.e.*,  $\Delta p_{a,b} \propto S$  to the leading order. We numerically verify the linear relation by systematically simulating an ensemble of a 3-neuron network (shown in Fig. 2a) with various value of  $S$  and estimating the corresponding value of  $\Delta p_{a,b}$ , as shown in the inset of Fig. 3a. Consequently, PTD-TE is proportional to  $S^2$ , with the numerical verification shown in Fig. 3a, which explains the reason that structural connectivity pattern in HH networks can be accurately inferred by PTD-TE values.

## PTD-TE overcomes the curse of dimensionality

We now demonstrate how PTD-TE overcomes the dimensionality problem faced by CTE and other methods by considering a pair of neurons,  $X$  and  $Y$ , in a  $(s + 2)$ -neuron recurrent network. In the traditional approach, estimating CTE (Eq. (1)) from  $X$  to  $Y$  requires estimating the joint probability distribution  $p(y_{n+1}, y_n^{(k)}, x_n^{(l)}, z_{1,n}^{(k_1)}, \dots, z_{s,n}^{(k_s)})$ . Consequently, the number of states in probability space grows exponentially with the dimensionality  $(k + l + 1 + \sum_{i=1}^s k_i)$  [12, 27, 51]. If we directly apply CTE to continuous-valued voltage time series, and we partition the range of neural voltage into  $p$  uniform bins for distribution estimation, then the total number of states becomes  $p^{k+l+1+\sum_{i=1}^s k_i}$ . This makes an accurate estimation of the probability distribution impractical with limited neural recording data, therefore resulting in the curse of dimensionality. In contrast, PTD-TE successfully overcomes the curse of dimensionality in four aspects, *i.e.*, small  $p$ , small  $k$ , small  $l$ , and zero  $k_i$ .

First, the binary state of the signals allows us to naturally set  $p = 2$ , which substantially reduces the dimension of the probability space.

Second, the binary state of the signals favors small  $k$ . In conventional TE-based reconstruction, the order  $k$  is introduced to prevent the mis-inference due to strong history dependent of a signal [12]. In general,  $k$  should be chosen at which the signal's auto-correlation function (ACF) decays to nearly zero, as shown in Fig. 1. For the binary time series from neuronal spiking activity, the ACF decays to near-zero within 1 ms (orange in Fig. 3b), which is significantly faster than for continuous-valued voltage time series (dark green in Fig. 3b). As near-zero ACF indicates uncorrelatedness to the signal's self-history, allowing the binary time series to be treated as independent random variables (see Ref. [52] that shows uncorrelatedness is equivalent to independence for binary random variables). This ensures the use of small  $k = \hat{k}$  in PTD-TE. In the resting part of this work, we choose  $\hat{k} = 1$  for reconstructing HH networks (with  $\hat{k}$  selected similarly for other nonlinear networks based on their ACFs).

Third, by introducing an additional time delay parameter, PTD-TE further reduces the order  $l$ . In conventional TE-based reconstruction,  $l$  must be chosen to cover the typical time-scale of the inter-neuronal interactions to distinguish connected neuronal pairs from unconnected ones. However, following the PTD-TE reconstruction pipeline (Fig. 1), PTD-TE scans over the time delay to find the optimal time delay that can maximize the ratio between connected and unconnected pairs with minimal  $l$ . Considering the 3-neuron system shown in Fig. 2a, with the optimal time delay  $\tau = 3$  ms, PTD-TE achieves the best reconstruction performance at  $l = 1$ , *i.e.* the ratio  $T_{X \rightarrow Y}^{\text{PTD}} / T_{X \rightarrow Z}^{\text{PTD}}$  reaches its maximum, which  $\tau = 0$  ms requires  $l \geq 5$  for comparable results, as shown in Fig. 3c. For the 3-neuron system in Fig. 2e, we obtain similar results in shown in Fig. 3d.

Finally, PTD-TE operates pairwise, eliminating the need to account for the state dimensionality of other neurons in the network. Again, for the 3-neuron system shown in Fig. 2a and e, CTE requires the information of neuron  $Y$  ( $X$ ) to exclude the indirect causal relation between  $X$  and  $Z$  ( $Y$  and  $Z$ ), introducing extra dimensionality. In contrast, PTD-TE inherently resists the influence of indirect causal effects, as evidenced by the accurate reconstructions in Fig. 2c and g. To understand this, we first analyze the relation between PTD-TE values for disconnected and connected neuron pairs in a chain motif (Fig. 2a). Without loss of generality, we express  $\Delta p_{a,b}^{X \rightarrow Z}$  as a double-variate function  $\Delta p_{a,b}^{X \rightarrow Z} = f(\Delta p_{a,b}^{X \rightarrow Y}, \Delta p_{a,b}^{Y \rightarrow Z})$ . By performing Taylor expansion with respect to coupling strengths  $S^{X \rightarrow Y}$  and  $S^{Y \rightarrow Z}$  and retaining the dominant terms (see *Methods*), we derive

$$\Delta p_{a,b}^{X \rightarrow Z} = O(\Delta p_{a,b}^{X \rightarrow Y} \cdot \Delta p_{a,b}^{Y \rightarrow Z}).$$



The numerical verification of this relation is shown in Fig. 3e. Notably, both  $\Delta p_{a,b}^{X \rightarrow Y}$  and  $\Delta p_{a,b}^{Y \rightarrow Z}$  of direct causality are very small (typically  $|\Delta p_{a,b}| < 0.01$  for  $\Delta t = 0.5$  ms calculated using parameters in neurophysiological regime). Consequently,  $\Delta p_{a,b}^{X \rightarrow Z}$  is much smaller than  $\Delta p_{a,b}^{X \rightarrow Y}$  and  $\Delta p_{a,b}^{Y \rightarrow Z}$ . Combining with Eq. (3),  $T_{X \rightarrow Z}$  (green circles) is negligible compared with  $T_{X \rightarrow Y}$  (blue dots) as shown in Fig. 3a. Therefore, although we calculate PTD-TE without conditioning on the information of intermediate nodes, the analysis shows that direct causal interactions can be distinguished from indirect ones, as verified numerically in Fig. 2. Similarly, for the confounder motif of  $Y \leftarrow X \rightarrow Z$ , we derive

$$\Delta p_{a,b}^{Y \rightarrow Z} = O(\Delta p_{a,b}^{X \rightarrow Y} \cdot \Delta p_{a,b}^{X \rightarrow Z}),$$

which is numerically verified in Fig. 3f. Here,  $\Delta p_{a,b}^{Y \rightarrow Z}$  is orders of magnitude smaller than  $\Delta p_{a,b}^{X \rightarrow Y}$  and  $\Delta p_{a,b}^{X \rightarrow Z}$ , ensuring that the PTD-TE values between commonly driven nodes are negligible compared to those with direct interactions.

Overall, to reconstruct a connection from  $X$  to  $Y$ , compared with the state number  $p^{k+l+1+\sum_i^s k_i}$  in CTE, PTD-TE reconstruction pipeline only requires estimating the joint probability with the state number  $2^{\hat{k}+1}$  ( $2^3$  for HH networks). This dramatic decrement of required state numbers makes the PTD-TE reconstruction applicable in practice.

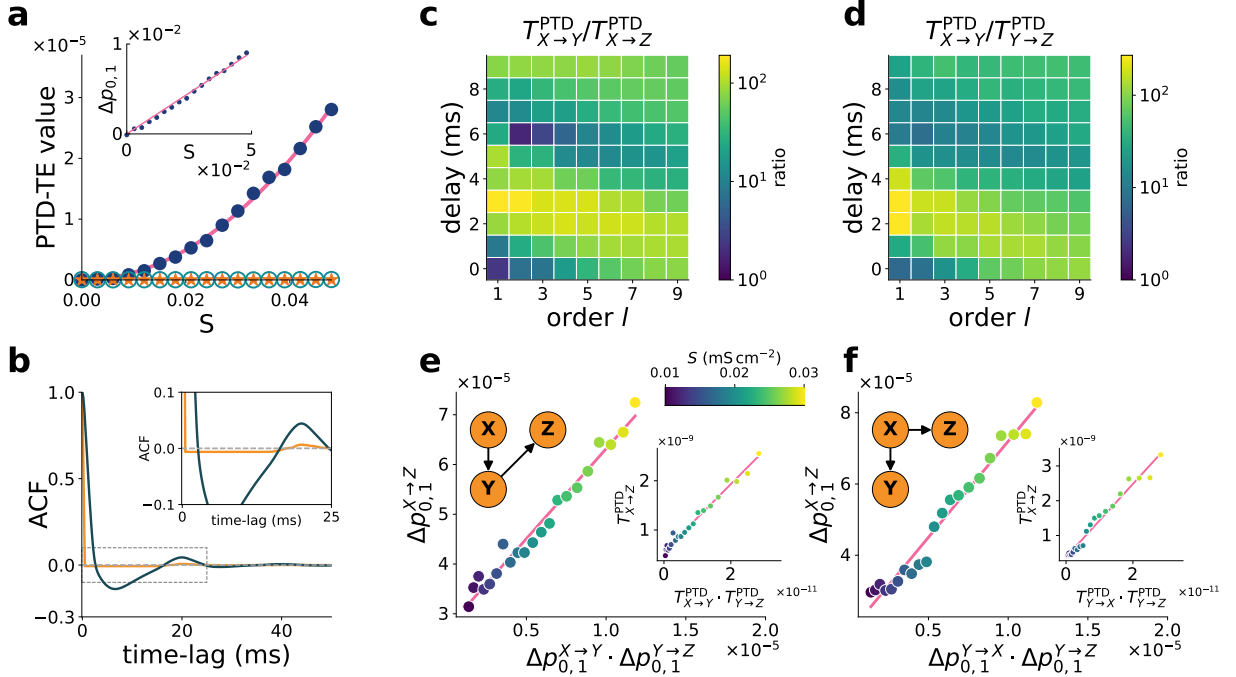


**Fig. 3** The mechanisms underlying PTD-TE reconstruction. **a**. PTD-TE values versus coupling strength  $S$  in 3-neuron HH networks with chain motifs (as in Fig. 2a). The blue dots, orange stars, and green circles indicate  $T_{X \rightarrow Y}^{\text{PTD}}$ ,  $T_{Y \rightarrow X}^{\text{PTD}}$ , and  $T_{X \rightarrow Z}^{\text{PTD}}$ , respectively. The pink line indicates a quadratic fit. Inset: linear relation between  $\Delta p_{0,1}$  and  $S$  from  $X$  to  $Y$  with the pink line reflecting a linear fit. **b**. ACF of (orange) binary spike-train data and (dark green) voltage time series of neuron  $X$ . Inset: the zoom of the region inside the dashed square in ACF plot. **c-d**. The ratio between PTD-TE values of connected and unconnected neuronal pairs (color coded) as varying order  $l$  and delay  $\tau$  in the 3-neuron HH system with chain motif (Fig. 2a) and confounder motif (Fig. 2e), respectively. **e-f**. The relation of  $\Delta p_{a,b}$  values between connected and unconnected pairs in the 3-neuron HH system with chain motif (Fig. 2a) and confounder motif (Fig. 2e). Inset: the relation between the corresponding PTD-TE values for those two types of neuronal pairs. The color of scatter plots indicates the homogeneous coupling strength  $S$  in networks. Spiking activity data with length 2.7 hours is used for computing PTD-TE values, with identical PTD-TE parameters as those in Fig. 2.

## Application of PTD-TE to large nonlinear networks

Previously, we demonstrated the underlying mechanism that enables successful PTD-TE reconstruction in small-scale networks. This theoretical framework naturally extends to larger network systems. To further validate its applicability, we next evaluate the performance of PTD-TE on large-scale networks, highlighting its potential for real-world applications. We simulate a 100-neuron HH network, randomly connected with 25% connection density. We simulate the network and record network activity for 2.7 hours ( $10^7$  ms), with the raster plot shown in Fig. 4a. Following the reconstruction pipeline in Fig. 1, we compute PTD-TE values of all neuronal pairs in the network, and the histogram (in log-scale) of PTD-TE values are shown in Fig. 4b. Here, we color the histogram of connected and unconnected pairs with orange and dark green, respectively, based on the ground truth connectivity (i.e., the adjacency matrix). The PTD-TE values of these two groups are clearly separated, demonstrating PTD-TE’s effectiveness as a metric for discriminating connected neuronal pairs. In practice, as the final step in the pipeline, we fit a double-mixture Gaussian mixture model (GMM) to PTD-TE values, and then get the optimal threshold for reconstruction, as shown by the pink line in Fig. 4a. As a result, the structural connectivity can be fully reconstructed with 100% of accuracy. We further evaluate the robustness of our PTD-TE reconstruction framework in the presense of measurement noise. To introduce temporal fluctuations in spike timing, we add uniformly distributed spike jitter between  $-2$  ms and  $2$  ms in spike times, as illustrated by the red marks in Fig. 4c. In Fig. 4d, PTD-TE remains highly effective with reconstruction accuracy 99.99%.

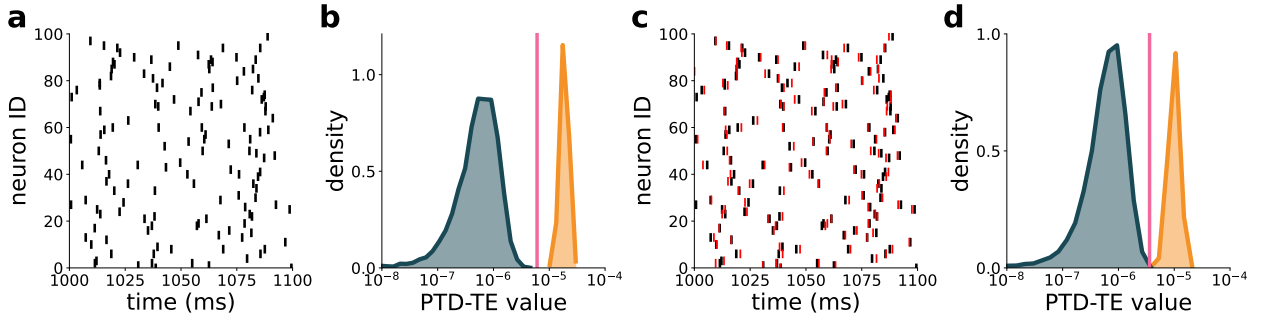


**Fig. 4** PTD-TE reconstruct large HH networks. **a.** The demo of raster plot for a 100-neuron HH network. **b.** The performance of PTD-TE-based reconstruction for the corresponding HH network in **a.** The PTD-TE distributions for connected and unconnected pairs are colored by orange and dark green, respectively, with pink line indicating the optimal reconstruction threshold determined by GMM (see *Methods*). **c.** The demo of jittered raster plot for the same 100-neuron HH network in **a.** Black and red marks indicate the original spike times and jittered spike times, respectively. **d.** The PTD-TE-based reconstruction performance using jittered spiking activity data. The color codes are defined similarly as those in **b.** PTD-TE parameters are chosen as  $k = l = 1$ ,  $\tau = 3$  ms.

As a model-free, information-theoretic measure, PTD-TE is broadly applicable to various types of nonlinear networks. To demonstrate its generality and robustness, we apply PTD-TE to four representative 100-node networks: the Lorenz network, logistic network, Rössler network, and linear recurrent neural network (LRNN). Each network has random connectivity with a density of 25% (see *Methods* for details on network dynamics). Notably, although these networks models do not inherently generate spikes, their continuous-valued time series can be converted into surrogate spike trains by applying appropriate thresholds.

In the Lorenz network, each node follows the Lorenz63 system [44]. We record the time series of the  $x$ -variable from each node and apply a threshold of  $x^{\text{th}} = 10$  (red dashed line in Fig. 5a, top) to generate surrogate spike trains (Fig. 5a, bottom). These spike trains are then binarized using a temporal resolution of  $\Delta t = 0.02$  ms, and the resulting binary time series are used as input to the PTD-TE pipeline, with parameters  $k = l = 1$  and  $\tau = 0$  ms. As shown in Fig. 5b, PTD-TE values for connected (orange) and unconnected (dark green) node pairs show clear separation, enabling reconstruction with 99.81% accuracy. The receiver operating characteristic (ROC) curve yields an area under the curve (AUC) of 0.99, indicating high reconstruction performance.

For the logistic network, each node evolves according to the discrete-time logistic map [46, 47]. The state  $x_i(n)$  is thresholded at  $x^{\text{th}} = 0.9$  (Fig. 5c) to produce spike trains, which are binarized using  $\Delta t = 1$ . With



PTD-TE parameters  $k = 2$ ,  $l = 1$ , and  $\tau = 0$ , the method yields perfect reconstruction (Fig. 5d), achieving 100% accuracy and an AUC of 1.

In the Rössler network, node dynamics follow the diffusive-coupled Rössler system [53]. We use the time series of the  $x_i(t)$  component for reconstruction, applying a threshold  $x^{\text{th}} = 8$  (Fig. 5e) and a binarization step of  $\Delta t = 3$  ms. Using PTD-TE parameters  $k = l = 5$  and  $\tau = 0$  ms, the method achieves 98.61% reconstruction accuracy, with an AUC of 0.99 (Fig. 5f).

Lastly, in the linear recurrent neural network (LRNN), we apply a threshold of  $x^{\text{th}} = 0.02$  to the node states (Fig. 5g) and binarize with  $\Delta t = 5$  ms. Using parameters  $k = 4$ ,  $l = 1$ , and  $\tau = 16$  ms, PTD-TE achieves 93.55% reconstruction accuracy (Fig. 5h), with an AUC of 0.98.

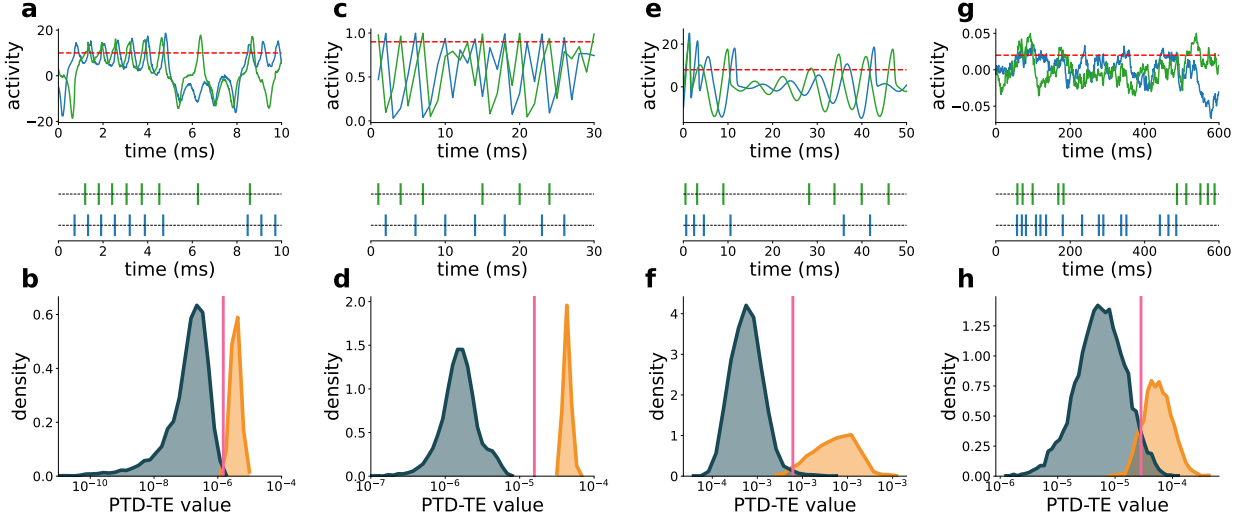


**Fig. 5** PTD-TE reconstruct the connectivity of general nonlinear networks. **a.** (Top) Continuous-valued activity time series of two example nodes from a 100-node Lorenz network. The red dashed line denotes the threshold value used for binarization in the PTD-TE pipeline. (Bottom) The corresponding surrogate spike trains for the same nodes. **b.** The PTD-TE-based reconstruction performance for the same Lorenz network. The PTD-TE distributions for connected and unconnected pairs are colored by orange and dark green, respectively, with pink line indicating the optimal reconstruction threshold determined by GMM (see *Methods*). **c-h.** Demonstration of binarization and reconstruction performance for (c-d) logistic network, (e-f) Rössler network, and (g-h) linear recurrent neural network (RNN), respectively, organized similarly as **a-b**. PTD-TE parameters are chosen as  $k = l = 1$ ,  $\tau = 0$  ms for Lorenz network,  $k = 2$ ,  $l = 1$ ,  $\tau = 0$  for logistic network,  $k = 5$ ,  $l = 5$ ,  $\tau = 0$  ms for Rössler network, and  $k = 4$ ,  $l = 1$ ,  $\tau = 5$  ms for linear RNN.

## Comparison with other network reconstruction methods

To further demonstrate the advantages of our method over other existing approaches, we next compare PTD-TE reconstruction with various popular methods for nonlinear network reconstruction, including symbolic transfer entropy [27], GLM for cross correlation (GLMCC) [54], dynamical differential covariance (DDC) [11, 55], convergent cross mapping (CCM) [56] and its related variations as frequency-domain CCM (FDCCM) and symbolic CCM (SCCM) [57, 58]. For fair comparison, all other methods are implemented in pairwise manner, except for DDC which relying on estimation of the inverse of network correlation matrix. We construct 8 different types of nonlinear networks and each includes 10 nodes with 25% connection density, including an excitatory HH network (HHEE), an excitatory-inhibitory mixed HH network (HHEI), an excitatory continuously coupled HH network (HHconEE), an excitatory-inhibitory mixed, continuously-coupled HH network (HHconEI), a Lorenz network, a logistic network, a Rössler network, and a linear recurrent neural network (LRNN) (see details in *Methods*).

We evaluate the reconstruction performances of all methods using the reconstruction accuracy and AUC values. As shown in Fig. 6a, PTD-TE reconstruction consistently outperforms other methods in all 8 network benchmarks, with AUC values being or approaching unity. For neuronal networks, except for PTD-TE and SCCM, all other methods give mis-inferred connections marked by blue squares in Fig. 6a. DDC performs

worst as it requires an accurate estimation of the derivative of voltage time series, and is more sensitive to the detection for inhibitory interactions. For non-neuronal networks, the performances for all other methods drops dramatically except for CCM and its variations. CCM-typed reconstruction and its variations are able to achieve slightly worse but comparable reconstruction performance as PTD-TE. However, CCM-typed methods fail in reconstructing the weakly coupled LRNN system due to the noise sensitivity of CCM-typed reconstructions.

The advantage of PTD-TE becomes more substantial when we evaluate the performance of these methods by reconstructing 10-node subnetworks, sampled from 100-node large networks, using noisy measurements of node activities. As shown in Fig. 6b, PTD-TE demonstrates the feasibility of subnetwork reconstruction and again consistently and dominantly outperforms other methods. Unlike the performance of other methods that drops with the increment of measuring noise, PTD-TE reconstruction possesses the robustness of performance against noisy measurements (Fig. 6c). Furthermore, the computational cost of PTD-TE mainly rely on the data loading and estimation joint probability distribution, which makes PTD-TE more efficient than all other reconstruction methods.

## Application of PTD-TE on real spike-train data

To investigate the applicability of PTD-TE to real data analysis, we now apply PTD-TE to spike trains recorded from multiple regions of mice cortex in order to reconstruct the underlying neuronal connectivity. Here we analyze the *Visual Coding Neuropixels* dataset and *Visual Behavior - Neuropixels* dataset that are publicly available from *Allen Brain Observatory* [48–50]. The former surveys spike trains mainly in visual cortices during passive viewing of visual stimuli, while the latter records the neuronal activity in mice performing the visual change detection tasks. We analyze spike-train recordings from 135 sessions (32 visual coding sessions and 103 visual behavior sessions). For each session, neurons with firing rates exceeding 0.05 Hz and signal-to-noise ratios above 4 are included. Spike trains are extracted under different stimulus or behavior conditions for separate reconstructions. In visual coding sessions, spike trains during passive viewing of drifting gratings, static gratings, natural scenes, and natural movies (each > 25 minutes) are analyzed. In visual behavior sessions, active and passive behavior periods (each > 1 hour) are examined separately.

Due to experimental limitations, ground-truth structural connectivity is unavailable. Thus, we quantify reconstruction performance using AUCs from double-mixture GMM fits to log-scaled PTD-TE values (see *Methods*). As shown in Fig. 7, the peak of AUC value distributions are around 0.9 for most sessions. Assuming structural connectivity of the neuronal network in the mice cortex remains stable within a session, we expect consistent reconstructed connectivity across conditions. Cross-condition of the consistency of reconstructed network exceeds 74% for the visual coding dataset and 69% for the visual behavior dataset, further supporting PTD-TE’s validity for real spike-train analysis.

## Discussion

In this work, we have introduced a general model-free network reconstruction pipeline based on the pairwise estimation of modified TE with time delays. Our framework effectively circumvents the curse of dimensionality inherent in conventional TE and CTE, which arises from the need for estimating high-dimensional probability distributions when reconstructing network structural connectivity. We also revealed a quadratic relationship between PTD-TE value and the coupling strength between nodes, providing a theoretical foundation for PTD-TE-based network reconstruction. We further demonstrated the orders of magnitude difference between PTD-TE values for connected and unconnected pairs, enabling accurate structural connectivity reconstruction. Our results showed that PTD-TE successfully reconstructs HH neuronal networks, as well as other nonlinear networks, including Lorenz networks, logistic networks, Rössler networks and linear recurrent neural networks, validating its underlying mechanism. Through comparisons with other methods across various networks, we demonstrated that PTD-TE consistently outperforms other methods, exhibiting its broad applicability to subnetwork reconstruction and robustness to noisy activity measurements. Finally, we applied PTD-TE to real spike-train data recorded from electrophysical experiments. High AUC values across all sessions, along with strong cross-condition consistency, further validate PTD-TE’s applicability to real experimental data.

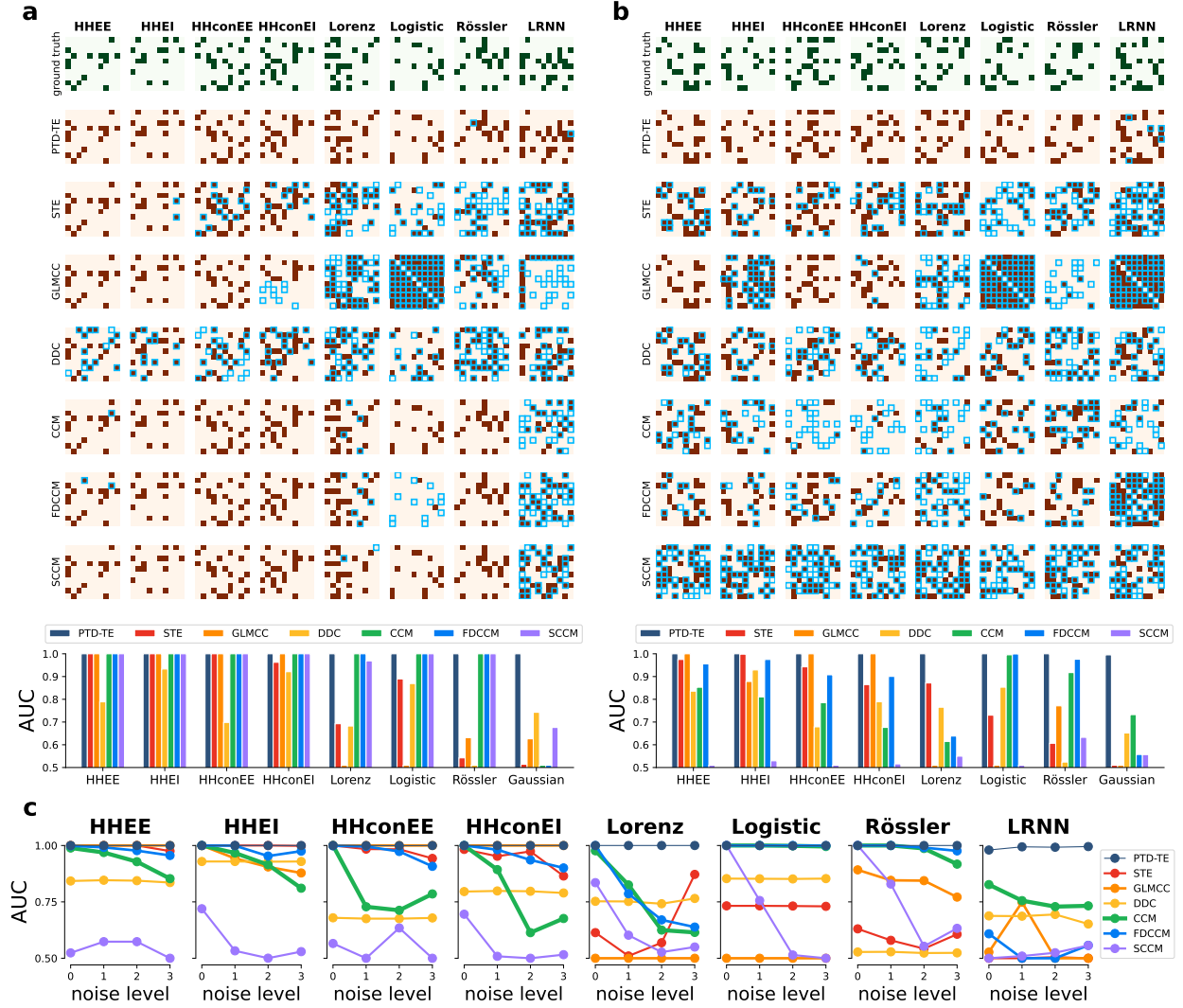


**Fig. 6** Reconstruction performances of multiple networks using different methods. **a**. Reconstructed adjacency matrices for 10-node networks (top) and corresponding AUC values (bottom). Top: the first row shows ground truth adjacency matrices for 8 benchmark networks, followed by reconstructed adjacency matrices (one method per line). Blue squares indicate either false positives or negatives. Reconstruction thresholds are determined by fitting GMMs to metrics (see *Methods*). **b**. Reconstructed adjacency matrices for 10-node subnetworks with measurement noise (top) and corresponding AUC values (bottom). Layout and color scheme match those in **a**. **c**. Relations between reconstruction AUC values and measurement noise levels contained in node activity time series. The reconstructions in **b** correspond to noise level 3. Color codes match those in **a-b** (bottom). PTD-TE parameters follow the standard reconstruction pipelines (Fig. 1).

It would be ideal to measure network structural connectivity directly. In neuroscience, the golden standard for assessing cellular-level structural connectivity involves techniques such as electron microscopic reconstruction of inter-neuronal synaptic structures or virus tracing [59–61]. However, these methods are either time- and resource-intensive or limited in their ability to reconstruct large numbers of neurons. In contrast, recent advances in electrophysiology and neural imaging, such as Neuropixel recordings [62, 63] and large-scale calcium imaging [64, 65], enable simultaneous cellular-level activity recordings from large neuron populations in behaving animals. These advancements open the possibility of inferring network structures using reconstruction methods, underscoring the importance of this work.

Compared to other types of neuronal recordings, spike-train data offers a high signal-to-noise ratio. Motivated by this, PTD-TE was initially developed for spike-train-based reconstructions and later extended

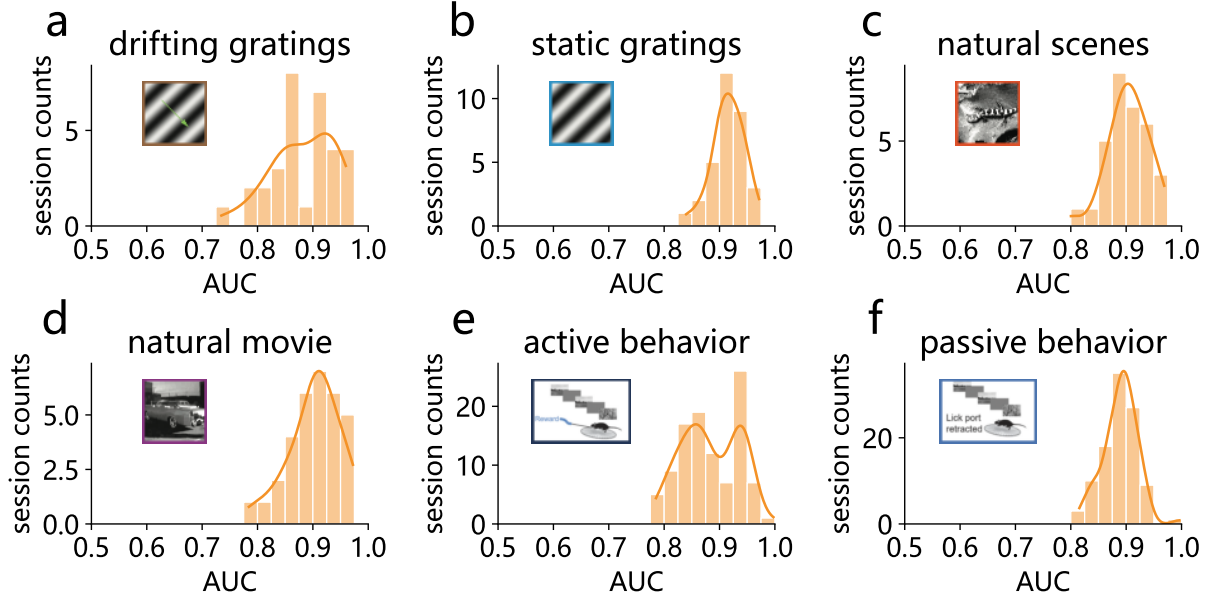


**Fig. 7** Performance of PTD-TE reconstruction using spike trains from mice data. **a-d.** Histograms of AUC values for reconstruction across sessions in the visual coding dataset for (a) drifting gratings, (b) static gratings, (c) natural scenes, and (d) natural movie, respectively. **e-f.** Histograms of AUC values for reconstructions across sessions in the visual behavior dataset under **e** active and **f** passive conditions. Orange lines indicate kernel density estimates of the histograms.

to general nonlinear systems. Unlike other methods focused on binary time series, PTD-TE fully leverages the advantageous properties of binary data in several ways. First, the binary state and short memory favor small order parameters, which reduces the dimensionality of PTD-TE estimation. Second, the direct interactions between binary time series ensure robustly large PTD-TE values against the effects of indirect interactions, enabling feasible pairwise reconstruction and enhancing its suitability for real-world applications. Third, unlike DDC and CCM, which are applied to continuous-valued time series and require smoothness in the recorded data, binarization acts as a filter for noisy subthreshold fluctuations, making PTD-TE robust to noisy measurements, as illustrated in Fig. 6c. When applied to other general nonlinear networks, a similar binarization process is employed with an appropriately chosen threshold for continuous-valued time series. As shown in Fig. 6, PTD-TE is broadly extendable to various physical networks, consistently achieving robust and reliable reconstruction performance.

Furthermore, PTD-TE remains effective even when coupling strengths in a network are heterogeneous, such as following a log-normal distribution, as observed in neuroscience experiments [66]. In such cases, PTD-TE achieves 99.26% accuracy in distinguishing directly connected from unconnected pairs, and the quadratic relationship between PTD-TE values and coupling strengths remains valid (see Fig. S1).

In general, it becomes challenging to infer the causal interactions when a network state becomes synchronous. However, PTD-TE achieves high reconstruction performance for networks with moderate synchronization, whether induced by strong recurrent interactions or coherent external stimuli. For example, in a quasi-synchronized HH network with strong coupling strength ( $S = 0.028 \text{ mS} \cdot \text{cm}^{-2}$ ), reconstruction accuracy reaches 99.53% using an additional down-sampling method (details in Fig. S2).

Despite its many advantages, PTD-TE requires sufficient data length for effective reconstruction, as a trade-off for the noise-filtering benefits of binarization. For instance, in a 100-neuron HH network (as shown in Fig. 5a), accurate reconstruction typically requires  $10^6$  ms of spike recordings, which is long but experimentally feasible. However, shorter data length reduces reconstruction performance (Fig. S3), highlighting the need for future work to improve performance with limited data. Additionally, PTD-TE's reconstruction performance declines as the contribution of indirect causal interactions increases, due to higher connection density or extremely strong coupling. Although PTD-TE values for indirect interactions are orders of magnitude smaller than those for direct interactions, they can accumulate with the growing number of indirect

paths (Fig. S4). Furthermore, denser networks exhibit more correlated and synchronized activity, which complicates reconstruction [67].

## Methods

### Network models

#### Hodgkin-Huxley neuronal network

The dynamics of the  $i$ -th Hodgkin-Huxley (HH) neuron's membrane potential  $V_i(t)$  is governed by

$$C\dot{V}_i = - (V_i - V_{\text{Na}})G_{\text{Na}}m_i^3h_i - (V_i - V_{\text{K}})G_{\text{K}}n_i^4 - (V_i - V_{\text{L}})G_{\text{L}} - (V_i - V_{\text{F}})G_i^{\text{F}} - (V_i - V_{\text{E}})G_i^{\text{E}} - (V_i - V_{\text{I}})G_i^{\text{I}}, \quad (4)$$

where  $C$  is the membrane capacitance.  $V_{\text{Na}}$ ,  $V_{\text{K}}$ , and  $V_{\text{L}}$  are the reversal potentials for the sodium current, potassium current, and leak current, respectively.  $G_{\text{Na}}$ ,  $G_{\text{K}}$ , and  $G_{\text{L}}$  are the corresponding maximum conductance of those ionic trans-membrane current. To capture the nonlinear gating effect of sodium and potassium ion channel, HH neuron has three gating variables,  $m_i$ ,  $h_i$ , and  $n_i$ , whose dynamics are defined by

$$\dot{z}_i = (1 - z_i)\alpha_z(V_i) - z_i\beta_z(V_i), \quad \text{for } z = m, h, n. \quad (5)$$

The forms of  $\alpha_z$  and  $\beta_z$  are defined by

$$\begin{aligned} \alpha_m(V) &= (0.1V + 4)/[1 - \exp(-0.1V - 4)], & \beta_m(V) &= 4 \exp[-(V + 65)/18], \\ \alpha_n(V) &= (0.01V + 0.55)/[1 - \exp(-0.1V - 5.5)], & \beta_n(V) &= 0.125 \exp[-(V + 65)/80], \\ \alpha_h(V) &= 0.07 \exp[-(V + 65)/20], & \beta_h(V) &= 1/[1 + \exp(-3.5 - 0.1V)]. \end{aligned} \quad (6)$$

The input synaptic current received by the HH neuron can be split into three parts, including feedforward input from the homogeneous Poisson processes, excitatory and inhibitory recurrent interactions from other neurons in the network.  $V_{\text{F}}$ ,  $V_{\text{E}}$ , and  $V_{\text{I}}$  are the corresponding reversal potential of those three types of current.  $G_i^{\text{F}}$ ,  $G_i^{\text{E}}$ , and  $G_i^{\text{I}}$  are their corresponding conductances, which are defined by

$$\begin{aligned} G_i^{\text{F}}(t) &= f \sum_k H(t - T_{ik}^{\text{F}}), \\ G_i^{\text{E}}(t) &= \sum_j^{N_E} A_{ij} S^{Q_i E} \sum_k H(t - T_{jk}), \\ G_i^{\text{I}}(t) &= \sum_j^{N_I} A_{ij} S^{Q_i I} \sum_k H(t - T_{jk}), \end{aligned} \quad (7)$$

where  $Q_i \in \{E, I\}$  denotes the type of the  $i$ -th neuron. Here,  $f$  is the strength of the Poisson process with rate  $\nu$ , and  $T_{ik}^{\text{F}}$  is the arrival time of the  $k$ -th Poisson spike for the  $i$ -th neuron. The temporal course of conductance change induced by a single Poisson spike is modeled by a double exponential function

$$H(t) = \frac{\sigma_r \sigma_d}{\sigma_d - \sigma_r} [\exp(-t/\sigma_d) - \exp(-t/\sigma_r)] \Theta(t), \quad (8)$$

where  $\sigma_r$  and  $\sigma_d$  are the rise and decay timescales, respectively, and  $\Theta(t)$  is the Heaviside function. The recurrent inputs are constrained by the structural connectivity of the network, defined by adjacency matrix  $\mathbf{A} = (A_{ij})$ , and the cell-type specific coupling strength  $S^{Q_i E}$  and  $S^{Q_i I}$  ( $Q_i$  is the type of the  $i$ -th neuron).  $T_{jk}$  is the arrival time of the  $k$ -th spike from the  $j$ -th neuron. The dynamics of spike-induced conductance evolution is also governed by Eq. (8). When the voltage  $V_i$ , described by Eqs. (4-8), exceeds the threshold  $V^{\text{th}}$  at  $T_{ik}$ , i.e.,

$$V_i(T_{ik}) = V^{\text{th}} \quad \text{and} \quad \dot{V}_i(T_{ik}) > 0,$$

we denote this event as the  $k$ -th spike of the  $i$ -th neuron. This triggers synaptic inputs to all its downstream neurons, as defined by Eqs. (7-8).

In this work, we choose parameters for simulating HH networks as listed below:  $C = 1 \mu\text{F} \cdot \text{cm}^{-2}$ ,  $V_{\text{Na}} = 50 \text{ mV}$ ,  $V_{\text{K}} = -77 \text{ mV}$ ,  $V_{\text{L}} = -54.387 \text{ mV}$ ,  $G_{\text{Na}} = 120 \text{ mS} \cdot \text{cm}^{-2}$ ,  $G_{\text{K}} = 36 \text{ mS} \cdot \text{cm}^{-2}$ ,  $G_{\text{L}} = 0.3 \text{ mS} \cdot \text{cm}^{-2}$ ,  $V_{\text{F}} = V_{\text{E}} = 0 \text{ mV}$ ,  $V_{\text{I}} = -80 \text{ mV}$ ,  $V^{\text{th}} = -50 \text{ mV}$ ,  $\sigma_r = 0.5 \text{ ms}$ ,  $\sigma_d = 3.0 \text{ ms}$ ,  $\nu = 0.15 \text{ ms}^{-1}$ ,  $f = 0.08 \text{ mS} \cdot \text{cm}^{-2}$ ,  $S^{EE} = S^{IE} = 0.02 \text{ mS} \cdot \text{cm}^{-2}$ , and  $S^{EI} = S^{II} = 0.08 \text{ mS} \cdot \text{cm}^{-2}$ . Time step  $\Delta t = 0.5 \text{ ms}$  is used in the binarization step of PTD-TE reconstruction. Unless otherwise specified, the typical data length for reconstructing the 100-neuron HH network is around 30 minutes ( $2 \times 10^6 \text{ ms}$ ), for instance, in Fig. 5a.

## Continuously coupled Hodgkin-Huxley neuronal network

The dynamics of the  $i$ -th continuously coupled HH neuron's membrane potential follows the same set of equations as in classical HH network (Eqs. 4 - 8), with the conductance of recurrent synaptic inputs (in Eq. 8) replaced by the smooth function [68, 69]

$$\begin{aligned} G_i^E &= \sum_j^{N_E} A_{ij} S^{Q_i E} \frac{1}{1 + \exp(-0.5V_j + 10)}, \\ G_i^I &= \sum_j^{N_I} A_{ij} S^{Q_i I} \frac{1}{1 + \exp(-0.5V_j + 10)}, \end{aligned} \quad (9)$$

where  $Q_i \in \{E, I\}$  denotes the type of the  $i$ -th neuron. Other parameters for continuously coupled HH networks are the same as those used in pulse-coupled HH networks. The threshold used for binarization is chosen as the same firing threshold  $V^{\text{th}} = -50 \text{ mV}$  as that in HH networks. In Fig. 6, time series length 2.7 hours ( $10^7 \text{ ms}$ ) are used to reconstruct the continuously coupled HH networks, with PTD-TE parameters set as  $k = 1$ ,  $l = 1$ ,  $\tau = 3 \text{ ms}$ , and binning time step  $\Delta t = 0.5 \text{ ms}$ , following the reconstruction pipeline.

## Lorenz Network

The dynamics of the  $i$ -th node in the pulse-coupled Lorenz networks is governed by [27, 44, 70, 71]

$$\begin{aligned} \dot{x}_i &= \sigma(y_i - x_i) + \sum_j A_{ij} S \sum_k \delta(t - T_{jk}), \\ \dot{y}_i &= \rho x_i - y_i - x_i z_i, \\ \dot{z}_i &= -\beta z_i + x_i y_i, \end{aligned} \quad (10)$$

where  $\sigma = 10$ ,  $\beta = 8/3$ ,  $\rho = 28$ ,  $S = 0.5$ , and  $\delta(\cdot)$  is the Dirac delta function. When  $x_j$  exceeds the threshold  $x^{\text{th}} = 10$  from below at time  $T_{jk}$ , node  $j$  immediately sends its  $k$ -th pulse to all of its post nodes ( $\{i | A_{ij} = 1\}$ ). Due to this pulse-coupled property, we naturally choose the same  $x^{\text{th}}$  as the binarization threshold in PTD-TE reconstruction pipeline, with a binning time step  $\Delta t = 0.02 \text{ ms}$ . In Figs. 5 and 6, time series of  $x$ -variable with length 17 minutes ( $10^6 \text{ ms}$ ) are used to reconstruct Lorenz networks. PTD-TE parameters are chosen as  $k = 1$ ,  $l = 1$ , and  $\tau = 0 \text{ ms}$  according to the PTD-TE pipeline.

## Logistic network

The dynamics of the  $i$ -th node in logistic networks are governed by the discrete time logistic map [46, 47]

$$X_i(n+1) = r X_i(n) [1 - X_i(n)] + \sum_j A_{ij} S \sum_k \tilde{\delta}_{n+1, T_{jk}}, \quad (11)$$

where  $r = 4$ ,  $S = 0.005$ , and  $\tilde{\delta}$  is the Kronecker delta function. We record  $T_{ik}$  as the discrete time point when  $X_i(T_{ik} - 1) < X^{\text{th}}$  and  $X_i(T_{ik}) \geq X^{\text{th}}$ , where  $X^{\text{th}} = 0.9$  is the emitting threshold. To apply PTD-TE, we convert  $X_i(n)$  to binary time series by setting the emitting threshold as the binarization threshold of  $X_i(n)$ , and choosing a binning time step  $\Delta t = 1$ . For reconstructions shown in Figs. 5 and 6, PTD-TE



parameters are chosen as  $k = 2, l = 1, \tau = 0$ , and time series of  $X_i(n)$  with length  $10^7$  time points are used for reconstruction.

### Rössler network

The dynamics of the  $i$ -th node of a diffusive-coupled Rössler system is defined by [27, 53, 71]

$$\begin{aligned}\dot{x}_i &= -y_i - z_i + \sum_{j \neq i}^N A_{ij} S \cdot (x_j - x_i) \\ \dot{y}_i &= x_i + ay_i \\ \dot{z}_i &= -b + z_i(x_i - c)\end{aligned}\tag{12}$$

where  $a = 0.25, b = 0.2, c = 10, S = 0.002$ . After simulating the Rössler network, we binarize  $x_i(t)$  to obtain binary time series by setting up a threshold  $x^{\text{th}} = 8$  and a binning time step  $\Delta t = 3$  ms, similarly as those for Lorenz networks. In Figs. 5 and 6, time series of  $x$ -variable with length 2.7 hours ( $10^7$  ms) are used to reconstruct Lorenz networks, with PTD-TE parameters set to  $k = 5, l = 5, \tau = 0$  ms.

### Linear recurrent neural network

The dynamics of the  $i$ -th node of a noise-driven linear recurrent neural network is described by

$$\tau_m \dot{x}_i = -x_i + S \sum_j A_{ij} x_j + \xi_i,\tag{13}$$

where  $\tau_m = 20$  ms is the time constant,  $S = 0.03$  is the coupling strength, and  $\xi_i$  is the independent and intrinsic Gaussian white noise for the  $i$ -th node with mean value  $\mu_\xi = 0$  and standard deviation value  $\sigma_\xi = 0.1$ . After simulating the network, we binarize  $x_i(t)$  to obtain binary time series  $T_i(k)$  by choosing a binarization threshold  $x^{\text{th}} = 0.02$  and a binning time step  $\Delta t = 5$  ms, similarly as those for Lorenz networks. In Figs. 5 and 6, time series of  $x_i(t)$  with length 27 hours ( $10^8$  ms) are used to reconstruct networks, with PTD-TE parameters set to  $k = 4, l = 1$ , and  $\tau = 5$  ms.

## Methods comparison

### Symbolic transfer entropy

Symbolic transfer entropy (STE) is an extension of conventional TE [27, 72]. Rather than operating on the continuous-valued activity time series, STE first transforms the historical state vectors  $y_n^{(k)}$  and  $x_n^{(l)}$  into symbolic sequences through a preprocessing step, and then compute the TE based on the resulting symbolized time series. In contrast to PTD-TE's binarization, STE incorporate the idea of delayed embedding to capture temporal by encoding them patterns as discrete symbols, which enhances its robustness to noise and non-stationarity compared with TE. For instance, for an order-5 history sequence of node  $x$ ,  $x_n^{(5)} = [-0.75, 0.90, -0.19, 0.72, -0.44]$ , the values are ranked in ascending order by their indices, resulting in the symbol "15342", where each digit reflects the position of the original entity in the sorted sequences. Moreover, this symbolization significantly reduces the size of the state space from  $5^5$  to  $5!$ , which helps mitigate the curse of dimensionality in estimating the joint probabilities. For comparison with PTD-TE, we use history lengths  $k = l = 5$  and continuous-valued time series with the identical data length as those used in PTD-TE's estimations for all networks in Fig. 6.

### GLMCC

GLMCC is a network reconstruction method specifically designed for analyzing the spike train data [54]. It combines cross-correlogram analysis with generalized linear model (GLM) methods to infer causal relationships between neurons. To estimate the effective connection from node  $X$  to node  $Y$ , GLMCC first computes

the cross-correlogram  $c_{X \rightarrow Y}(t)$  from the binarized time series (as generated in the PTD-TE processing pipelines). It then fits a GLM of the form

$$c(\tau) = \exp(a(\tau) + J_{YX}f(\tau) + J_{XY}f(-\tau)),$$

where  $J_{YX}$  represents the effective coupling strength from node  $X$  to  $Y$ , vice versa. The function  $f(\tau)$  models the spike-induced modulation of spike counts via an exponential kernel, while  $a(t)$  captures background influences as slow-wave drives. Typically, by fitting  $J_{YX}$ , GLMCC quantifies both strength and sign (i.e., excitatory or inhibitory) of the effective interaction from  $X$  to  $Y$ . For our comparison, we adapt the Python implementation and hyperparameter settings reported in its original work [54]. For the HH networks, we compute GLMCC using data with the same length as used in PTD-TE cases. For the other networks, we used one-tenth of the full data length to reduce computational costs, which scale with the number of spike events in the binarized time series.

### Dynamical differential correlation (DDC)

DDC estimates structural connectivity by integrating differential information with partial covariance analysis [55]. The DDC-inferred connectivity matrix is computed as:

$$W^{\text{DDC}} = \text{cov}(\dot{\mathbf{x}}, \mathbf{x}) \text{cov}(\mathbf{x}, \mathbf{x})^{-1} \quad (14)$$

where  $\text{cov}(\cdot, \cdot)$  denotes the covariance matrix. Conceptually, the first term captures the directional (driver-driven) interactions through the relationship between a node's derivative and the activity of other nodes, while the second term serves to mitigate the influence of common inputs. DDC is particularly effective at identifying inhibitory causal interactions from relatively short recordings, but it relies on accurate estimation of time derivatives, which can make it sensitive to noise. For a fair comparison with other methods evaluated in this study, we used the same data length for DDC-based reconstruction across all networks as that used in PTD-TE.

### Convergence cross mapping (CCM) and its variations

CCM infers causal relationships based on the theory of state-space reconstruction [56, 73, 74]. Given discrete time series  $\{x_n\}$  and  $\{y_n\}$  from node  $X$  and  $Y$ , respectively, we define the order- $l$  delay coordinate (DC) vectors as follows:

$$\mathbf{X}(n) := [x_n, x_{n-1}, \dots, x_{n-l+1}]^\top, \quad \mathbf{Y}(n) := [y_n, y_{n-1}, \dots, y_{n-l+1}]^\top.$$

These vectors form delay-embedding manifolds  $\mathbf{M}_X := \{\mathbf{X}(t) | t \in [l-1, L]\}$  and  $\mathbf{M}_Y := \{\mathbf{Y}(t) | t \in [l-1, L]\}$  in the state space. If  $X$  causally drives  $Y$ , the information about  $\mathbf{M}_X$  should be reflected in  $\mathbf{M}_Y$ , enabling the prediction of  $\mathbf{M}_X$  based on the local geometry of  $\mathbf{M}_Y$ . Practically, for the  $n$ -th delayed embedding state of  $Y$ ,  $\mathbf{Y}(n)$ , we identify its  $l+1$  nearest neighbors in the state space, denoted as  $\mathbf{Y}(n_1), \dots, \mathbf{Y}(n_{l+1})$ , with the discrete time index from  $n_1$  to  $n_{l+1}$ . Then, we predict  $x_n$ , the  $n$ -th state of  $X$ , using the information of  $\mathbf{Y}(n)$ 's neighbors:

$$\hat{x}_n = \sum_{i=1}^{l+1} w_i x_{n_i}, \quad (15)$$

where  $n_i$  refers to the time index of  $i$ -th nearest neighbor of  $\mathbf{Y}(n)$  in the state space. The weight  $w_i$  is defined as

$$w_i = u_i / \sum_{j=1}^{l+1} u_j, \quad u_i = \exp \left( - \frac{\|\mathbf{Y}(n) - \mathbf{Y}(n_i)\|}{\|\mathbf{Y}(n) - \mathbf{Y}(n_1)\|} \right). \quad (16)$$

where  $\|\cdot\|$  represents the Euclidean distance in the state space. Intuitively, if  $X$  causally influences  $Y$ , clusters of states on  $\mathbf{M}_Y$  should map onto corresponding clusters on  $\mathbf{M}_X$ . Therefore,  $x_n$  can be predicted using the information from the local structure of clusters on  $\mathbf{M}_Y$ . As the data length  $L$  increases, the prediction  $\hat{x}_n$  is

expected to converge to the true  $x_n$ . In our implementation, we quantify the effective connection from  $X$  to  $Y$  using the Pearson correlation coefficient between  $\{x_n\}$  and  $\{\hat{x}_n\}$ .

In addition, to address the sensitivity of CCM to noise, we also evaluate two recent variants of CCM: Frequency-Domain CCM (FDCCM) [57] and Symbolic CCM (SCCM) [58]. FDCCM operates on DC vectors constructed in the frequency-domain, while SCCM replaces the original DC vectors with symbolic permutation, similar to the symbolization step in STE.

Due to the high computational cost of the  $k$ -nearest neighbor search in CCM-based methods, we used one-tenth of the full time series length compared with PTD-TE reconstructions for all CCM, FDCCM, and SCCM reconstructions shown in Fig. 6, to balance computational efficiency and performance.

## Performance criteria

### Simulation data

For any of the reconstruction pipeline, the network’s adjacency matrix is inferred by applying an optimal threshold of the corresponding causality values, determined by fitting a GMM to the distribution of causality values across all node pairs. The alignment between the reconstructed adjacency matrix and the ground truth connectivity is quantified as the reconstruction accuracy, which is reported for each network. To further evaluate the sensitivity and specificity of the reconstruction, we employ receiver operating characteristic (ROC) curve analysis. The area under the ROC curve (AUC) serves as a key metric, measuring how effectively the method distinguishes directly connected pairs from disconnected ones. An AUC close to 1 indicates a clear separation between the metric values of directly connected and disconnected pairs, reflecting excellent reconstruction performance. Conversely, an AUC near 0.5 suggests overlapping distributions of metric values, implying performance comparable to random guessing. It is worth noting that some methods, such as GLMCC and DDC, yield both positive and negative metric values, with the latter often interpreted as indicative of inhibitory interactions. Since our evaluation focuses on reconstructing the presence or absence of connections (regardless of sign), we compute performance metrics based on the absolute values of these measures.

### Real spike-train data

When working with real spike train data, the ground truth structural connectivity is typically unknown, making it difficult to directly evaluate reconstruction performance. However, prior experimental evidence suggests that coupling strengths in the mouse and monkey brains follow a log-normal distribution [66]. Motivated by this finding, we fit a GMM to the log-transformed distribution of PTD-TE values. The two resulting Gaussian mixtures are treated as proxies for the true distributions of connected and unconnected pairs, respectively. Based on these fitted distributions, we perform ROC-AUC analysis to quantify the method’s ability to distinguish between the two classes, as illustrated in Fig. 7.

## Details about PTD-TE-based network reconstruction pipeline

**Step 1:** Convert continuous-valued time series to binary time series. For a continuous-valued time series  $x(t)$ , if  $x(\hat{t}) = x^{\text{th}}$  and  $\dot{x}(\hat{t}) > 0$ , we define  $T_k = \hat{t}$  as the spike time of the  $k$ -th pulse event, where  $x^{\text{th}}$  is the binarization threshold. Using a discrete time step  $\Delta t$ , we define a binary time series  $S^x(n)$ , where  $S^x(n) = 1$  if a pulse event occurs within  $((n-1)\Delta t, n\Delta t]$ , otherwise  $S^x(n) = 0$ .  $\Delta t$  is chosen such that at most one pulse appears within each time step. Inspired by action potential generation, we define pulse-output events for general continuous-valued time series using a threshold.

**Step 2:** Determine the order parameter  $k$  (for the target node). For a  $k$ -th order Markov process,  $k$  conditions out information transfer from the target’s own history. In practice,  $k$  is chosen as the time lag  $\hat{k}$  where the absolute value of the autocorrelation function (ACF) of  $S^x(n)$  drops below 0.1, *i.e.*,

$$\hat{k} = \arg \min_k |\text{ACF}_{S^x(n)}(k)| < 0.1|.$$

**Step 3:** Determine the optimal time delay  $\tau$ . Scan and choose  $\tau$  as  $\hat{\tau}$  which maximize  $T_{X \rightarrow Y}^{\text{PTD}}(\hat{k}, l = 1, \tau)$ . Notably,  $\hat{\tau}$  reflects the typical timescale of synaptic interactions.

**Step 4:** Determine the order parameter  $l$  (for the source node). With the optimal  $\tau$ ,  $l = 1$  suffices for most cases. Larger  $l$  values are suitable for systems with slower, persistent interactions. In practice, scan  $l$  values from 1 to 10 to optimize reconstruction performance. In this work,  $l = 1$  is used for all networks except the Rössler network and real spike trains ( $l = 5$ ).

**Step 5:** Determine the classification threshold. After computing PTD-TE values for all pairs in a network using the parameters chosen in Steps 1–4, fit a double-mixture Gaussian mixture model (GMM) to the PTD-TE values. The two Gaussian distributions represent the PTD-TE distributions for connected and disconnected pairs, respectively. The threshold is chosen such that the probabilities of belonging to either Gaussian distribution are equal.

**Acknowledgments.** This work was supported by Science and Technology Innovation 2030 - Brain Science and Brain-Inspired Intelligence Project with Grant No. 2021ZD0200204 (S. Li, D. Zhou); Shanghai Municipal Commission of Science and Technology with Grant No. 24JS2810400 (S. Li, D. Zhou); National Natural Science Foundation of China Grant 12271361, 12250710674 (S. Li); National Natural Science Foundation of China with Grant No. 12225109 (D. Zhou) and the Student Innovation Center at Shanghai Jiao Tong University (K. Chen, Z.K. Tian, Y. Chen, S. Li, D. Zhou)

## Declarations

- Conflict of interest: The authors have no relevant financial or non-financial interests to disclose.
- Data and code availability: Data and code will be made available based on reasonable requests.

## References

- [1] Suárez, L. E., Markello, R. D., Betzel, R. F. & Misic, B. Linking structure and function in macroscale brain networks. *Trends in Cognitive Sciences* **24**, 302–315 (2020).
- [2] Boers, N., Kurths, J. & Marwan, N. Complex systems approaches for Earth system data analysis. *Journal of Physics: Complexity* **2**, 011001 (2021).
- [3] Friston, K., Harrison, L. & Penny, W. Dynamic causal modelling. *NeuroImage* **19**, 1273–1302 (2003).
- [4] Zhou, D., Zhang, Y., Xiao, Y. & Cai, D. Reliability of the Granger causality inference. *New J. Phys.* **16**, 043016 (2014).
- [5] Seth, A. K., Barrett, A. B. & Barnett, L. Granger causality analysis in neuroscience and neuroimaging. *Journal of Neuroscience* **35**, 3293–3297 (2015).
- [6] Mehdizadehfar, V., Ghassemi, F., Fallah, A., Mohammad-Rezazadeh, I. & Pouretmad, H. Brain connectivity analysis in fathers of children with autism. *Cognitive Neurodynamics* **14**, 781–793 (2020).
- [7] Strogatz, S. H. Exploring complex networks. *nature* **410**, 268 (2001).
- [8] Guelzim, N., Bottani, S., Bourguin, P. & Képès, F. Topological and causal structure of the yeast transcriptional regulatory network. *Nature genetics* **31**, 60 (2002).
- [9] Székely, G. J., Rizzo, M. L. *et al.* Partial distance correlation with methods for dissimilarities. *The Annals of Statistics* **42**, 2382–2412 (2014).
- [10] Tian, Z.-q. K., Chen, K., Li, S., McLaughlin, D. W. & Zhou, D. Causal connectivity measures for pulse-output network reconstruction: Analysis and applications. *Proceedings of the National Academy of Sciences* **121**, e2305297121 (2024).

- [11] Laasch, N., Braun, W., Knoff, L., Bielecki, J. & Hilgetag, C. C. Comparison of derivative-based and correlation-based methods to estimate effective connectivity in neural networks. *Scientific Reports* **15**, 5357 (2025).
- [12] Schreiber, T. Measuring information transfer. *Physical review letters* **85**, 461 (2000).
- [13] Honey, C. J., Kötter, R., Breakspear, M. & Sporns, O. Network structure of cerebral cortex shapes functional connectivity on multiple time scales. *Proceedings of the National Academy of Sciences* **104**, 10240–10245 (2007).
- [14] Vicente, R., Wibral, M., Lindner, M. & Pipa, G. Transfer entropy—a model-free measure of effective connectivity for the neurosciences. *Journal of Computational Neuroscience* **30**, 45–67 (2011).
- [15] Spinney, R. E., Prokopenko, M. & Lizier, J. T. Transfer entropy in continuous time, with applications to jump and neural spiking processes. *Physical Review E* **95**, 032319 (2017).
- [16] Ito, S. *et al.* Extending Transfer Entropy Improves Identification of Effective Connectivity in a Spiking Cortical Network Model. *PLoS ONE* **6**, e27431 (2011).
- [17] Bossomaier, T., Barnett, L., Harré, M. & Lizier, J. T. *Transfer Entropy*, 65–95 (Springer International Publishing, Cham, 2016).
- [18] Ver Steeg, G. & Galstyan, A. *Information transfer in social media*, 509–518 (ACM, Lyon France, 2012).
- [19] Li, J., Liang, C., Zhu, X., Sun, X. & Wu, D. Risk contagion in Chinese banking industry: A Transfer Entropy-based analysis. *Entropy. An International and Interdisciplinary Journal of Entropy and Information Studies* **15**, 5549–5564 (2013).
- [20] Varley, T. F., Sporns, O., Schaffelhofer, S., Scherberger, H. & Dann, B. Information-processing dynamics in neural networks of macaque cerebral cortex reflect cognitive state and behavior. *Proceedings of the National Academy of Sciences* **120**, e2207677120 (2023).
- [21] Friston, K. J. Functional and effective connectivity in neuroimaging: A synthesis. *Human brain mapping* **2**, 56–78 (1994).
- [22] Bressler, S. L. & Seth, A. K. Wiener–Granger causality: A well established methodology. *Neuroimage* **58**, 323–329 (2011).
- [23] Chen, Y., Rangarajan, G., Feng, J. & Ding, M. Analyzing multiple nonlinear time series with extended granger causality. *Physics Letters A* **324**, 26–35 (2004).
- [24] Zhou, D., Xiao, Y., Zhang, Y., Xu, Z. & Cai, D. Causal and structural connectivity of pulse-coupled nonlinear networks. *Physical review letters* **111**, 054102 (2013).
- [25] Barnett, L., Barrett, A. B. & Seth, A. K. Granger Causality and Transfer Entropy Are Equivalent for Gaussian Variables. *Physical Review Letters* **103**, 238701 (2009).
- [26] Wiener, N. The theory of prediction. *Modern mathematics for engineers* (1956).
- [27] Staniek, M. & Lehnertz, K. Symbolic Transfer Entropy. *Physical Review Letters* **100**, 158101 (2008).
- [28] Kugiumtzis, D. Partial transfer entropy on rank vectors. *The European Physical Journal* **222**, 401–420 (2013).
- [29] Wibral, M. *et al.* Measuring Information-Transfer Delays. *PLoS ONE* **8**, e55809 (2013).

- [30] Kraskov, A., Stögbauer, H. & Grassberger, P. Estimating mutual information. *Physical Review E* **69**, 066138 (2004).
- [31] Gómez-Herrero, G. *et al.* Assessing Coupling Dynamics from an Ensemble of Time Series. *Entropy* **17**, 1958–1970 (2015). URL <http://www.mdpi.com/1099-4300/17/4/1958>.
- [32] Wibral, M., Vicente, R. & Lindner, M. in *Transfer Entropy in Neuroscience* (eds Wibral, M., Vicente, R. & Lizier, J. T.) *Directed Information Measures in Neuroscience* Understanding Complex Systems, 3–36 (Springer Berlin Heidelberg, 2014). URL [http://link.springer.com/10.1007/978-3-642-54474-3\\_1](http://link.springer.com/10.1007/978-3-642-54474-3_1).
- [33] Lee, J. *et al.* Transfer Entropy Estimation and Directional Coupling Change Detection in Biomedical Time Series. *BioMedical Engineering OnLine* **11**, 19 (2012).
- [34] Darmon, D. & Rapp, P. E. Specific transfer entropy and other state-dependent transfer entropies for continuous-state input-output systems. *Physical Review E* **96**, 022121 (2017).
- [35] Verdes, P. F. Assessing causality from multivariate time series. *Physical Review E* **72**, 026222 (2005). URL <https://link.aps.org/doi/10.1103/PhysRevE.72.026222>.
- [36] Lizier, J. T., Prokopenko, M. & Zomaya, A. Y. Local information transfer as a spatiotemporal filter for complex systems. *Physical Review E* **77**, 026110 (2008). URL <https://link.aps.org/doi/10.1103/PhysRevE.77.026110>.
- [37] Papan, A., Kugiumtzis, D. & Larsson, P. G. DETECTION OF DIRECT CAUSAL EFFECTS AND APPLICATION TO EPILEPTIC ELECTROENCEPHALOGRAM ANALYSIS. *International Journal of Bifurcation and Chaos* **22**, 1250222 (2012). URL <https://www.worldscientific.com/doi/abs/10.1142/S0218127412502227>.
- [38] Runge, J., Heitzig, J., Petoukhov, V. & Kurths, J. Escaping the Curse of Dimensionality in Estimating Multivariate Transfer Entropy. *Physical Review Letters* **108**, 258701 (2012).
- [39] Runge, J., Heitzig, J., Marwan, N. & Kurths, J. Quantifying causal coupling strength: A lag-specific measure for multivariate time series related to transfer entropy. *Physical Review E* **86**, 061121 (2012).
- [40] Sipahi, R. & Porfiri, M. Improving on transfer entropy-based network reconstruction using time-delays: Approach and validation. *Chaos: An Interdisciplinary Journal of Nonlinear Science* **30**, 023125 (2020).
- [41] Hodgkin, A. L. & Huxley, A. F. A quantitative description of membrane current and its application to conduction and excitation in nerve. *The Journal of physiology* **117**, 500–544 (1952).
- [42] Kistler, W. M., Gerstner, W. & van Hemmen, J. L. Reduction of the Hodgkin-Huxley equations to a single-variable threshold model. *Neural computation* **9**, 1015–1045 (1997).
- [43] Pospischil, M. *et al.* Minimal Hodgkin–Huxley type models for different classes of cortical and thalamic neurons. *Biological cybernetics* **99**, 427–441 (2008).
- [44] Lorenz, E. N. Deterministic nonperiodic flow. *Journal of Atmospheric Sciences* **20**, 130–148 (1963).
- [45] Anishchenko, V. S., Silchenko, A. N. & Khovanov, I. A. Synchronization of switching processes in coupled Lorenz systems. *Physical Review E* **57**, 316–322 (1998).
- [46] May, R. M. Simple mathematical models with very complicated dynamics. *Nature* **261**, 459–467 (1976).
- [47] Dickten, H. & Lehnertz, K. Identifying delayed directional couplings with symbolic transfer entropy. *Physical Review E* **90**, 062706 (2014).



- [48] Siegle, J. H. *et al.* Survey of spiking in the mouse visual system reveals functional hierarchy. *Nature* **592**, 86–92 (2021).
- [49] Allen Institute MindScope Program. Allen Brain Observatory – Neuropixels Visual Coding [dataset]. Available from [brain-map.org/explore/circuits](https://portal.brain-map.org/explore/circuits) (2019).
- [50] Allen Institute MindScope Program. Allen Brain Observatory – Neuropixels Visual Behavior [dataset]. Available from <https://portal.brain-map.org/circuits-behavior/visual-behavior-neuropixels> (2022).
- [51] Amornbunchornvej, C., Zheleva, E. & Berger-Wolf, T. Variable-lag Granger Causality and Transfer Entropy for Time Series Analysis. *ACM Transactions on Knowledge Discovery from Data* **15**, 1–30 (2021).
- [52] Zhang, K. Bet on independence. *Journal of the American Statistical Association* **114**, 1620–1637 (2019).
- [53] Rössler, O. An equation for continuous chaos. *Physics Letters A* **57**, 397–398 (1976).
- [54] Kobayashi, R. *et al.* Reconstructing neuronal circuitry from parallel spike trains. *Nature Communications* **10**, 1–13 (2019).
- [55] Chen, Y., Rosen, B. Q. & Terrence J. Sejnowski. Dynamical differential covariance recovers directional network structure in multiscale neural systems. *Proceedings of the National Academy of Sciences* **119**, e2117234119 (2022).
- [56] Sugihara, G. *et al.* Detecting Causality in Complex Ecosystems. *Science* **338**, 496–500 (2012).
- [57] Avvaru, S. & Parhi, K. K. Effective Brain Connectivity Extraction by Frequency-Domain Convergent Cross-Mapping (FDCCM) and Its Application in Parkinson’s Disease Classification. *IEEE Transactions on Biomedical Engineering* **70**, 2475–2485 (2023).
- [58] Ge, X. & Lin, A. Symbolic convergent cross mapping based on permutation mutual information. *Chaos, Solitons & Fractals* **167**, 112992 (2023).
- [59] The MICrONS Consortium *et al.* Functional connectomics spanning multiple areas of mouse visual cortex. *Nature* **640**, 435–447 (2025).
- [60] Xu, F. *et al.* High-throughput mapping of a whole rhesus monkey brain at micrometer resolution. *Nature Biotechnology* **39**, 1521–1528 (2021).
- [61] Markov, N. T. *et al.* A Weighted and Directed Interareal Connectivity Matrix for Macaque Cerebral Cortex. *Cerebral Cortex* **24**, 17–36 (2014).
- [62] Jun, J. J. *et al.* Fully integrated silicon probes for high-density recording of neural activity. *Nature* **551**, 232–236 (2017).
- [63] Steinmetz, N. A. *et al.* Neuropixels 2.0: A miniaturized high-density probe for stable, long-term brain recordings. *Science* **372**, eabf4588 (2021).
- [64] Grienberger, C., Giovannucci, A., Zeiger, W. & Portera-Cailliau, C. Two-photon calcium imaging of neuronal activity. *Nature Reviews Methods Primers* **2**, 67 (2022).
- [65] Vladimirov, N. *et al.* Light-sheet functional imaging in fictively behaving zebrafish. *Nature Methods* **11**, 883–884 (2014).
- [66] Buzsáki, G. & Mizuseki, K. The log-dynamic brain: How skewed distributions affect network operations. *Nature Reviews Neuroscience* **15**, 264–278 (2014).

- [67] Das, A. & Fiete, I. R. Systematic errors in connectivity inferred from activity in strongly recurrent networks. *Nature Neuroscience* **23**, 1286–1296 (2020).
- [68] Compte, A., Sanchez-Vives, M. V., McCormick, D. A. & Wang, X.-J. Cellular and network mechanisms of slow oscillatory activity ( $\leq 1$  Hz) and wave propagations in a cortical network model. *Journal of neurophysiology* **89**, 2707–2725 (2003).
- [69] Sun, Y., Zhou, D., Rangan, A. V. & Cai, D. Pseudo-Lyapunov exponents and predictability of Hodgkin-Huxley neuronal network dynamics. *Journal of computational neuroscience* **28**, 247–266 (2010).
- [70] Belykh, I., Belykh, V. & Hasler, M. Synchronization in asymmetrically coupled networks with node balance. *Chaos (Woodbury, N.Y.)* **16**, 15102 (2006).
- [71] Paluš, M. & Vejmelka, M. Directionality of coupling from bivariate time series: How to avoid false causalities and missed connections. *Physical Review E* **75**, 056211 (2007).
- [72] Martini, M., Kranz, T. A., Wagner, T. & Lehnertz, K. Inferring directional interactions from transient signals with symbolic transfer entropy. *Physical Review E* **83**, 011919 (2011).
- [73] Ye, H., Deyle, E. R., Gilarranz, L. J. & Sugihara, G. Distinguishing time-delayed causal interactions using convergent cross mapping. *Scientific Reports* **5**, 14750 (2015).
- [74] Mønster, D., Fusaroli, R., Tylén, K., Roepstorff, A. & Sherson, J. F. Causal inference from noisy time-series data — Testing the Convergent Cross-Mapping algorithm in the presence of noise and external influence. *Future Generation Computer Systems* **73**, 52–62 (2017).

## Supplementary information.

## Supplementary Texts

### Derivation for the relation between PTD-TE and coupling strength

For a two-node system with connection  $X \rightarrow Y$ , the PTD-TE from  $X$  to  $Y$  is defined by Eq. 2. We first map the binary state of  $y_n^{(k)}$  and  $x_{n-\tau}^{(l)}$  to decimal numbers. For an individual realization of  $y_n^{(k)} = (y_n, y_{n-1}, \dots, y_{n-k+1})$ , its decimal number representation is

$$\sum_{i=1}^k y_{n+1-i} \cdot 2^{k-i}$$

We give the following notations

$$\begin{aligned} p(a, b) &= p(y_n^{(k)} = a, x_{n-\tau}^{(l)} = b) & p(a) &= p(y_n^{(k)} = a) \\ p_{a,b} &= p(y_{n+1} = 1 | y_n^{(k)} = a, x_{n-\tau}^{(l)} = b) & \Delta p_{a,b} &= p_{a,b} - p_{a,0}, \end{aligned} \quad (17)$$

where  $a$  and  $b$  are decimal numbers representing  $y_n^{(k)}$  and  $x_{n-\tau}^{(l)}$ , respectively. Then, we rewrite Eq. (2) in the form of  $p(a, b)$ ,  $p_{a,b}$  and  $\Delta p_{a,b}$  as

$$\begin{aligned} T_{X \rightarrow Y}^{\text{PTD}} &= \sum_{a,b} \left[ \underbrace{p_{a,b} p(a, b) \cdot \log \left( \frac{p_{a,b}}{\sum_b p_{a,b} \cdot p(a, b)} \right)}_{\text{given } y_{n+1}=1} + \underbrace{(1 - p_{a,b}) p(a, b) \cdot \log \left( \frac{1 - p_{a,b}}{\sum_b (1 - p_{a,b}) p(a, b)} \right)}_{\text{given } y_{n+1}=0} \right] \\ &= - \sum_{a,b} \left[ p_{a,b} p(a, b) \cdot \log \left( 1 + \frac{-\Delta p_{a,b} p(a) + \sum_b \Delta p_{a,b} p(a, b)}{p_{a,b} \cdot p(a)} \right) \right. \\ &\quad \left. + (1 - p_{a,b}) p(a, b) \cdot \log \left( 1 + \frac{\Delta p_{a,b} p(a) - \sum_b \Delta p_{a,b} p(a, b)}{(1 - p_{a,b}) \cdot p(a)} \right) \right]. \end{aligned} \quad (18)$$

Since  $\Delta p_{a,b}$  represents the  $X$ 's activity induced change of state probability of  $y_{n+1} = 1$ , and the change is proportional to the synaptic strength which is rather weak in neurophysiological regime (numerically shown in the inset of Fig. 3a),  $\Delta p_{a,b}$  should be a small quantity, and Eq. (18) can be expanded with respect to  $\Delta p_{a,b}$ ,

$$\begin{aligned} T_{X \rightarrow Y}^{\text{PTD}} &= - \sum_{a,b} \left[ p_{a,b} p(a, b) \left( \frac{-\Delta p_{a,b} p(a) + \sum_b \Delta p_{a,b} p(a, b)}{p_{a,b} \cdot p(a)} - \frac{(-\Delta p_{a,b} p(a) + \sum_b \Delta p_{a,b} p(a, b))^2}{2 p_{a,b}^2 \cdot p(a)^2} \right) \right. \\ &\quad \left. + (1 - p_{a,b}) p(a, b) \left( \frac{\Delta p_{a,b} p(a) - \sum_b \Delta p_{a,b} p(a, b)}{(1 - p_{a,b}) \cdot p(a)} - \frac{(\Delta p_{a,b} p(a) - \sum_b \Delta p_{a,b} p(a, b))^2}{2 (1 - p_{a,b})^2 \cdot p(a)^2} \right) + o(\Delta p_{a,b}^2) \right] \\ &= \frac{1}{2} \sum_{a,b} \frac{p(a, b)}{p_{a,b} (1 - p_{a,b})} \left( \Delta p_{a,b}^2 - 2 \frac{\Delta p_{a,b} (\sum_b \Delta p_{a,b} p(a, b))}{p(a)} + \frac{(\sum_b \Delta p_{a,b} p(a, b))^2}{p(a)^2} \right) + o(\Delta p_{a,b}^2) \\ &= \frac{1}{2} \sum_a \frac{1}{p_{a,0} - p_{a,0}^2} \sum_b \left[ p(a, b) \left( \Delta p_{a,b}^2 - 2 \frac{\Delta p_{a,b} (\sum_b \Delta p_{a,b} p(a, b))}{p(a)} + \frac{(\sum_b \Delta p_{a,b} p(a, b))^2}{p(a)^2} \right) + o(\Delta p_{a,b}^2) \right] \\ &= \frac{1}{2} \sum_a \frac{1}{p_{a,0} - p_{a,0}^2} \left[ \sum_b p(a, b) \Delta p_{a,b}^2 - 2 \frac{(\sum_b \Delta p_{a,b} p(a, b))^2}{p(a)} + p(a) \frac{(\sum_b \Delta p_{a,b} p(a, b))^2}{p(a)^2} + o(\Delta p_{a,b}^2) \right] \\ &= \frac{1}{2} \sum_a \frac{1}{p_{a,0} - p_{a,0}^2} \left( \sum_b p(a, b) \Delta p_{a,b}^2 - \frac{(\sum_b p(a, b) \Delta p_{a,b})^2}{p(a)} \right) + o(\Delta p_{a,b}^2). \end{aligned} \quad (19)$$

So far, according to Eq. (19), we identify the quadratic relationship between  $T_{X \rightarrow Y}$  and  $\Delta p_{a,b}$ .

Next, we demonstrate that  $\Delta p_{a,b}$  in Eq. (19) further depends on the structural coupling strength  $S$ . Without loss of generality,  $\Delta p_{a,b}$  can be represented as a function of  $S$ , *i.e.*,  $\Delta p_{a,b} = f(S)$ . Expanding  $\Delta p_{a,b}$

in terms of  $S$  yields

$$\begin{aligned}\Delta p_{a,b} &= f(0) + f'(0)S + \frac{1}{2}f''(0)S^2 + o(S^2) \\ &= f'(0)S + \frac{1}{2}f''(0)S^2 + o(S^2).\end{aligned}\tag{20}$$

The last equality in Eq. (20) holds because  $\Delta p_{a,b} = 0$  when  $S = 0$ . Therefore, in the weakly coupled case (synaptic strength in neurophysiological regime),  $\Delta p_{a,b}$  is proportional to  $S$  at leading order. Consequently, combining Eq. (19) and (20), we show that PTD-TE is proportional to  $S^2$ , as numerically verified in Fig. 3a.

## Derivation for the relation between PTD-TE values of connected and unconnected pairs

We demonstrate that PTD-TE can accurately identify directly connected pairs from others. For the three-neuron HH network with chain motif in Fig. 2a, we show that the PTD-TE value  $T_{X \rightarrow Z}^{\text{PTD}}$  is orders of magnitude smaller than  $T_{X \rightarrow Y}^{\text{PTD}}$  (or  $T_{Y \rightarrow Z}^{\text{PTD}}$ ). Assume that the coupling strength from  $X$  to  $Y$  and from  $Y$  to  $Z$  are  $S_1$  and  $S_2$ , respectively, the  $X$ 's spike induced change of firing probability of  $Z$ ,  $\Delta p_{a,b}^{X \rightarrow Z}$  should depend on both  $S_1$  and  $S_2$ , *i.e.*,  $\Delta p_{a,b}^{X \rightarrow Z} = g(S_1, S_2)$ . Treating  $S_1$  and  $S_2$  as small quantities,  $g(S_1, S_2)$  can be Taylor expanded as

$$\Delta p_{a,b}^{X \rightarrow Z} = g(0,0) + \left. \frac{\partial g}{\partial S_1} \right|_{(0,0)} S_1 + \left. \frac{\partial g}{\partial S_2} \right|_{(0,0)} S_2 + \frac{1}{2} \left. \frac{\partial^2 g}{\partial S_1^2} \right|_{(0,0)} S_1^2 + \frac{1}{2} \left. \frac{\partial^2 g}{\partial S_2^2} \right|_{(0,0)} S_2^2 + \frac{1}{2} \left. \frac{\partial^2 g}{\partial S_1 \partial S_2} \right|_{(0,0)} S_1 S_2 + o(S_1 S_2).$$

Since  $\Delta p_{a,b}^{X \rightarrow Z}$  is nonzero if and only if both  $S_1$  and  $S_2$  are nonzero, its leading term is the bilinear product of  $S_1$  and  $S_2$ , *i.e.*,

$$\Delta p_{a,b}^{X \rightarrow Z} = \frac{1}{2} \left. \frac{\partial^2 g}{\partial S_1 \partial S_2} \right|_{(0,0)} S_1 S_2 + o(S_1 S_2).\tag{21}$$

Since  $\Delta p^{X \rightarrow Y} \propto O(S_1)$  and  $\Delta p^{Y \rightarrow Z} \propto O(S_2)$ , we have

$$\Delta p^{X \rightarrow Z} = O(\Delta p^{X \rightarrow Y} \cdot \Delta p^{Y \rightarrow Z})$$

by retaining the dominant term in the expansion. In networks with coupling strengths in the neurophysiological regime, both  $\Delta p_{a,b}^{X \rightarrow Y}$  and  $\Delta p_{a,b}^{Y \rightarrow Z}$  for direct connections are relatively small. As shown in the inset of Fig. 3a in the main text, these values are typically less than 0.01 for the HH network. Consequently, the indirect increment  $\Delta p_{a,b}^{X \rightarrow Z}$  is significantly smaller than  $\Delta p_{a,b}^{X \rightarrow Y}$ , a result numerically confirmed in Fig. 3c (left). Combined with the derived relation in Eq. (19),  $T_{X \rightarrow Z}$  is orders of magnitude smaller than  $T_{X \rightarrow Y}$ . This ensures robust differentiation between direct and indirect interactions, preventing false positive inferences. The orders of magnitude difference between  $T_{X \rightarrow Z}$  and  $T_{X \rightarrow Y}$  is further validated in the inset of Fig. 3c (left). Similarly, for the confounder motif (Fig. 2e), we can also derive that  $\Delta p^{Y \rightarrow Z} = O(\Delta p^{X \rightarrow Y} \cdot \Delta p^{X \rightarrow Z})$ , which is verified numerically in Fig. 3c (right) (inset: corresponding PTD-TE relations).

In summary, unlike conventional TE and CTE, PTD-TE based on binary time series effectively distinguishes the effective connectivity arising from direct physical interactions versus indirect ones. Importantly, it achieves this without relying on information about the third node, ensuring robust and effective network reconstruction.

## Supplementary Figures

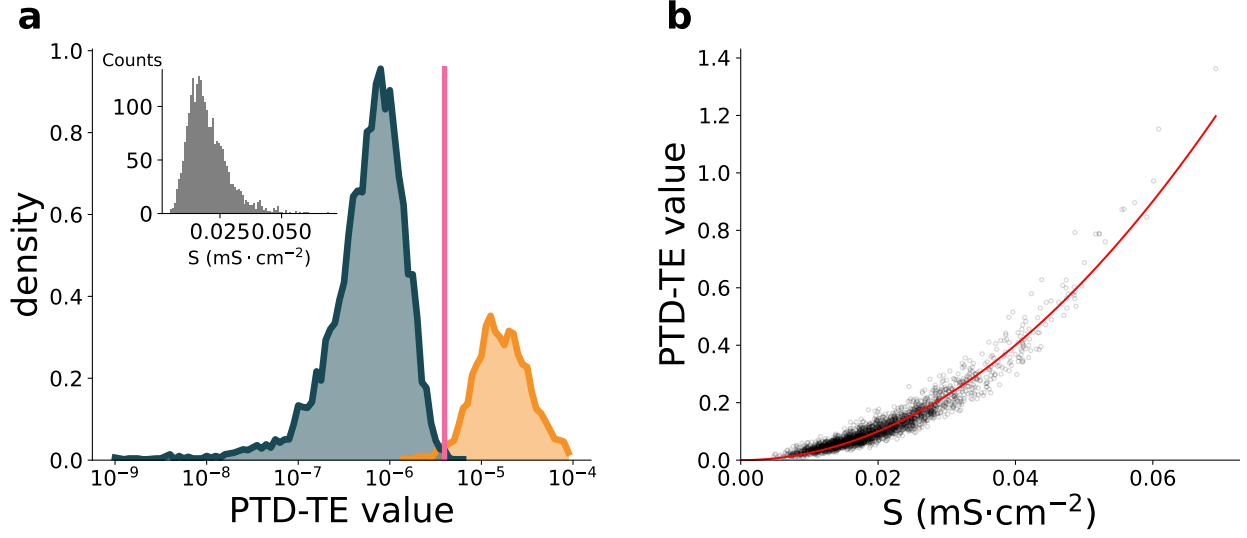


**Fig. S1** PTD-TE reconstruction of an HH network with log-normally distributed structural connectivity. **a.** The distribution of PTD-TE values. PTD-TE parameters are set to  $k = l = 1$ ,  $\tau = 3$  ms, the same as in Fig. 4 in the main text. Orange and dark green corresponds to PTD-TE values of connected and unconnected pairs, respectively. The pink line indicates the optimal reconstruction threshold, achieving 99.26% reconstruction accuracy. Inset: Histogram of log-normally distributed coupling strengths  $S$  in the network, and remaining parameters for the HH network simulation match those in 100-neuron HH networks in the main text. **b.** PTD-TE values versus coupling strength  $S$ . The quadratic relation between PTD-TE and  $S$  also valid for networks with heterogeneous structural connectivity. The red solid line is a quadratic fit with  $R^2 = 0.94$ .

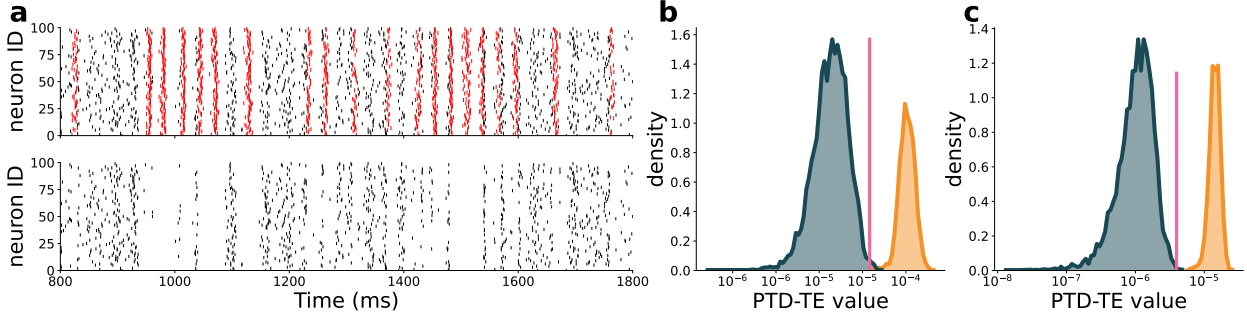


**Fig. S2** Reconstructions for HH networks in near synchronous regime. **a.** The raster plot of an HH network HH in quasi-synchronous regime with strong recurrent coupling ( $S = 0.028 \text{ mS} \cdot \text{cm}^{-2}$ ) (top) before and (bottom) after down-sampling. All spikes are uniformly binned, with 10 ms bin size, into time series  $r(t)$  to quantify the synchronization level, where  $r(k)$  is the total number of spikes in the network in  $k$ -th time bin. We denote  $k$ -th bin as the synchronized bins if  $r(k) \geq \langle r \rangle + 0.5 \sigma(r)$ , where  $\langle r \rangle$  and  $\sigma(r)$  are the mean and standard deviation of spike counts within single bin over time. To improve the inference performance for networks in quasi-synchronous state, the down-sampling operation removes spikes within synchronized time bins, indicated by red bars in the top subfigure. **b.** The distribution of PTD-TE values for the same HH network in **a.** **c.** The distribution of PTD-TE values for another quasi-synchronous HH network, induced by moderate correlated Poisson inputs (35% input correlation with strength  $f = 0.2 \text{ mS} \cdot \text{cm}^{-2}$  and frequency  $\nu = 0.05 \text{ ms}^{-1}$ ), after similar down-sampling preprocessing. PTD-TE parameters are chosen as  $k = l = 1$ ,  $\tau = 3$  ms,  $\Delta t = 0.5$  ms in **c-d**. The adjacency matrices for structural connectivity are the same as in Fig. 4. Orange and dark green curves are corresponding to PTD-TE values of connected and unconnected pairs, respectively. Pink lines indicate the optimal thresholds, resulting 99.53% and 99.93% reconstruction accuracy for **c** and **d**, respectively.

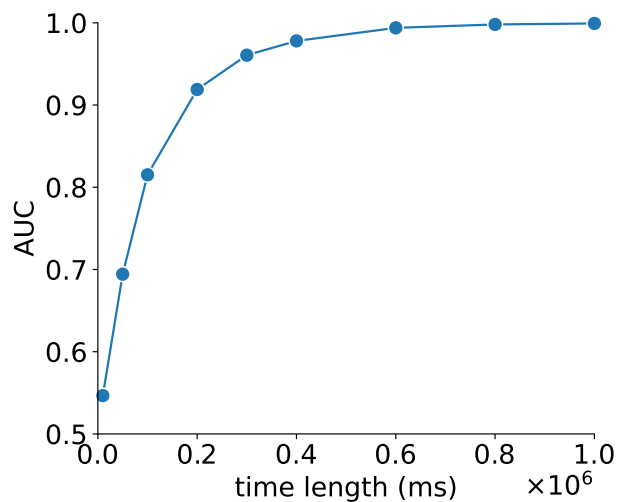


**Fig. S3** Relation between reconstruction performance and the data length used.

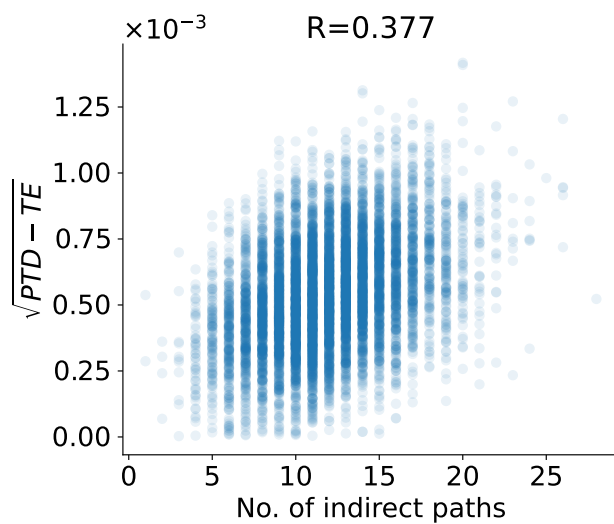


**Fig. S4** Relation between PTD-TE and the number of indirect interaction paths (both chain and confounder motifs are included) for unconnected pairs. The correlation between  $\sqrt{PTD - TE}$  and number of indirect paths is 0.377.

## Supplementary Tables



Network	PTD-TE	STE	GLMCC	DDC	CCM	FDCCM	SCCM
HHEE	<b>1.000</b>	1.000	1.000	0.789	1.000	1.000	1.000
HHEI	<b>1.000</b>	1.000	1.000	0.933	1.000	1.000	1.000
HHconEE	<b>1.000</b>	1.000	1.000	0.698	1.000	1.000	1.000
HHconEI	<b>1.000</b>	0.963	1.000	0.921	1.000	1.000	1.000
Lorenz	<b>1.000</b>	0.693	0.422	0.682	1.000	1.000	0.969
Rössler	<b>1.000</b>	0.542	0.631	0.481	1.000	1.000	1.000
Logistic	<b>1.000</b>	0.890	0.500	0.869	1.000	1.000	1.000
LRNN	<b>1.000</b>	0.522	0.626	0.743	0.499	0.472	0.676

**Table 1** Reconstruction performance (AUC) of 10-node networks.

Network	PTD-TE	STE	GLMCC	DDC	CCM	FDCCM	SCCM
HHEE	<b>1.000</b>	1.000	1.000	0.843	0.989	0.999	0.524
HHEI	<b>1.000</b>	1.000	1.000	0.929	1.000	1.000	0.720
HHconEE	<b>1.000</b>	1.000	1.000	0.679	1.000	0.999	0.566
HHconEI	<b>1.000</b>	0.983	1.000	0.796	1.000	1.000	0.695
Lorenz	<b>1.000</b>	0.614	0.459	0.753	0.977	1.000	0.835
Rössler	<b>1.000</b>	0.630	0.892	0.528	1.000	1.000	1.000
Logistic	<b>1.000</b>	0.732	0.500	0.853	1.000	1.000	1.000
LRNN	<b>0.980</b>	0.479	0.527	0.688	0.827	0.608	0.448

**Table 2** Reconstruction performance (AUC) of 10-node subnetworks sampled from 100-node large networks.

Network	PTD-TE	STE	GLMCC	DDC	CCM	FDCCM	SCCM
HHEE	<b>1.000</b>	0.975	1.000	0.836	0.853	0.956	0.491
HHEI	<b>1.000</b>	0.998	0.878	0.929	0.811	0.975	0.529
HHconEE	<b>1.000</b>	0.943	1.000	0.679	0.785	0.908	0.423
HHconEI	<b>1.000</b>	0.865	1.000	0.790	0.676	0.901	0.516
Lorenz	<b>1.000</b>	0.872	0.479	0.765	0.615	0.638	0.550
Rössler	<b>1.000</b>	0.606	0.771	0.524	0.917	0.976	0.633
Logistic	<b>1.000</b>	0.730	0.500	0.853	0.996	0.999	0.452
LRNN	<b>0.995</b>	0.534	0.500	0.652	0.733	0.557	0.557

**Table 3** Reconstruction performance (AUC) of 10-node subnetworks, sampled from 100-node large networks, based on noisy measurements of activity time series